AGU PUBLICATIONS

JGR

Journal of Geophysical Research: Solid Earth

RESEARCH ARTICLE

10.1002/2017JB015052

Special Section:
Slow Slip Phenomena and Plate Boundary Processes

Key Points:
- SAF LFEs are apparently triggered by the tides
- Diffusivity is constrained by the tidal correlation
- Friction, dilatancy, and effective stress are also constrained

Correspondence to:
N. M. Beeler,
nbeeler@usgs.gov

Citation:
Beeler, N. M., Thomas, A., Bürgmann, R., & Shelly, D. (2018). Constraints on friction, dilatancy, diffusivity, and effective stress from low-frequency earthquake rates on the deep San Andreas Fault. *Journal of Geophysical Research: Solid Earth*, *123*, 583–605. https://doi.org/10.1002/2017JB015052

Received 28 SEP 2017
Accepted 3 OCT 2017
Accepted article online 15 DEC 2017
Published online 27 JAN 2018

Constraints on Friction, Dilatancy, Diffusivity, and Effective Stress From Low-Frequency Earthquake Rates on the Deep San Andreas Fault

N. M. Beeler[1], **Amanda Thomas**[2], **Roland Bürgmann**[3], **and David Shelly**[4]

[1]US Geological Survey Cascades Observatory, Vancouver, WA, USA, [2]Department of Earth Sciences, University of Oregon, Eugene, OR, USA, [3]Earth and Planetary Science, University of California, Berkeley, CA, USA, [4]US Geological Survey Volcano Science Center, Menlo Park, CA, USA

Abstract Families of recurring low-frequency earthquakes (LFEs) within nonvolcanic tremor on the San Andreas Fault in central California are sensitive to tidal stresses. LFEs occur at all levels of the tides, are strongly correlated and in phase with the ~200 Pa shear stresses, and weakly and not systematically correlated with the ~2 kPa tidal normal stresses. We assume that LFEs are small sources that repeatedly fail during shear within a much larger scale, aseismically slipping fault zone and consider two different models of the fault slip: (1) modulation of the fault slip rate by the tidal stresses or (2) episodic slip, triggered by the tides. LFEs are strongly clustered with duration much shorter than the semidiurnal tide; they cannot be significantly modulated on that time scale. The recurrence times of clusters, however, are many times longer than the semidiurnal, leading to an appearance of tidal triggering. In this context we examine the predictions of laboratory-observed triggered frictional (dilatant) fault slip. The undrained end-member model produces no sensitivity to the tidal normal stress, and slip onsets are in phase with the tidal shear stress. The tidal correlation constrains the diffusivity to be less than ~1×10^{-6}/s and the product of the friction and dilatancy coefficients to be at most 5×10^{-7}, orders of magnitude smaller than observed at room temperature. In the absence of dilatancy the effective normal stress at failure would be about ~55 kPa. For this model the observations require intrinsic weakness, low dilatancy, and lithostatic pore fluid.

1. Introduction

Deep slip on some plate-boundary scale faults is accompanied by nonvolcanic tremor (NVT), long duration seismic signals with highest signal-to-noise ratios in the ~2–8 Hz band, of similar frequency to volcanic tremor (Obara, 2002). The seismic moment of the tremor has been estimated to be a fraction of the total moment of the deep slip (Kao et al., 2010). Individual repeating low-frequency earthquakes (LFEs) make up a portion of the tremor (Shelly et al., 2007), and the LFE focal mechanisms are consistent with shear slip on the plate boundary (Ide et al., 2007). Accordingly, a simple, popular conceptual model for LFEs is that they represent radiation emanating from small, persistent regions that repeatedly fail during aseismic shear of the larger-scale surrounding fault zone (Shelly et al., 2007).

In this paper we study the sensitivity of NVT to imposed changes in stress from the tides using LFEs extracted from the tremor on the deep San Andreas Fault (SAF) in central California (Shelly & Hardebeck, 2010) and consider two models of the relation between tidal stress and fault slip. The LFEs locate between 16 and 29 km depth, meaning this seismicity occurs above the MOHO (~30 km depth) but beneath the depth extent where conventional earthquakes predominately occur. For short-hand throughout we refer to the region containing the LFEs generically as the "transition" zone between brittle and ductile deformation because deformation in this region shows evidence of both smaller scale seismic (low-frequency earthquakes) and larger scale aseismic (creep) behavior. Here LFE occurrence, and the NVT generally, is sensitive to tidal shear stress changes as small as fractions of a kilopascal (Thomas et al., 2009, 2012). LFEs occur at all phases of the tides, and the maximum rate of occurrence coincides approximately with the maximum tidal shear stress, with peak-to-peak amplitude less than 0.5 kPa (Thomas et al., 2009, 2012). Following Thomas et al. (2012), in Figure 1, LFEs from 4/2001 to 2/2012 are binned according to the tidal right-lateral shear stress on the SAF at the time of LFE occurrence. The number of events in each bin (N_{obs}) is normalized by the expected number of events (N_{exp}), assuming LFEs are randomly distributed in time. The expected number is the total number of events in the catalog divided by the fractional catalog time at that bin's range of tidal stress. $N_{obs}/N_{exp} > 1$

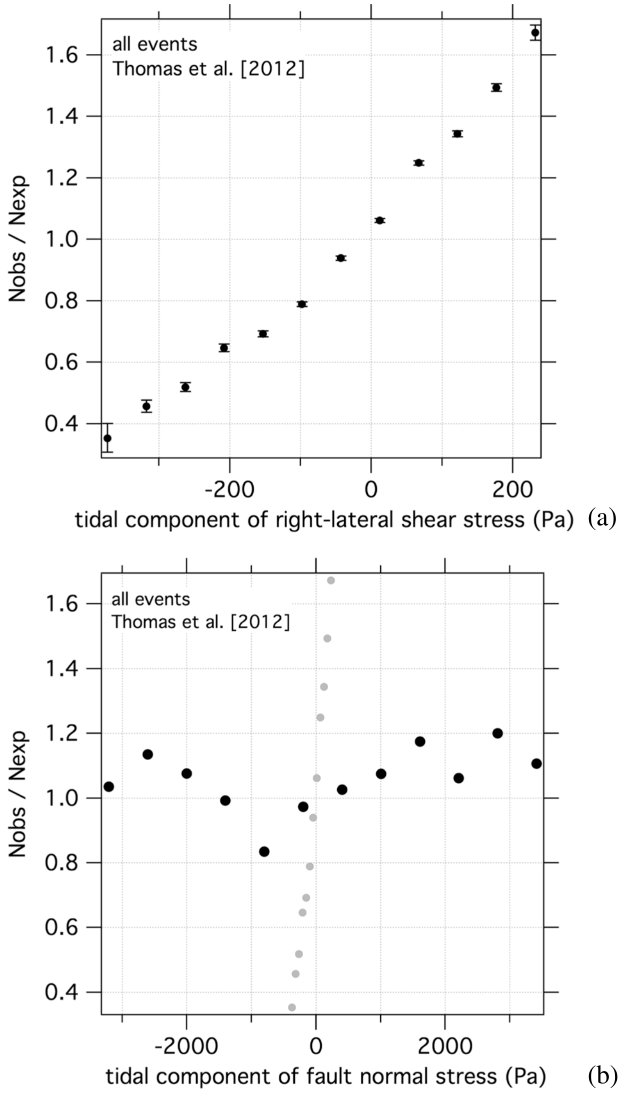

Figure 1. Relation between earthquake occurrence and the tidal shear stress from Thomas et al. (2012) for ~732,000 events in 88 LFE families. (a) The left vertical axis is the observed number of events normalized by the expected number. The error bars are the 99% bootstrap confidence intervals. The horizontal axis is the tidal shear stress. (b) Same as Figure 1a for fault normal stress. Shown for reference are the shear stress data from Figure 1a (small gray symbols).

denote an excess of LFEs at that stress level, and $N_{obs}/N_{exp} < 1$ indicate a deficit. The collective event occurrence rate varies systematically from low but nonzero at the lowest and negative tidal shear stress to high at the highest, positive stress (Figure 1a). NVT on the SAF shows the same relationship (see Figure 3 of Thomas et al., 2009). In contrast, collectively, LFEs show no strong or systematic relationship with the tides resolved as normal stress on the SAF (Figure 1b). In detail for individual families there is rather complex relation to normal stress, including apparent correlation with both positive and negative normal stress; see the detailed results in Thomas et al. (2012). In any case, the correlation of LFE occurrence and the normal stress tides never comes close to that of the shear stress, and for our purposes, the collective sensitivity depicted in Figures 1a and 1b well describes the contrast. This is surprising because the solid Earth tidal strains are largely volumetric and the peak amplitude of the normal stress tide is more than 10 times larger than that of the shear stress. In the following we use this sensitivity to the shear stress and the lack of coherent sensitivity to normal stress as constraints on the fault rheology.

We evaluate two models of frictional fault slip for their implications for the correlations between the tides and low-frequency earthquake occurrence. In the immediately following section 1.1, the two models are briefly described: a slip modulation model where the aseismic fault slip rate is affected directly by the tidal stress, and a triggered slip model where slip occurs episodically and the onsets of slip events are triggered by the tides. In the two subsequent sections 2 and 3 the models are described in more detail, starting with a slip modulation model in section 2, where two previously published modulation models (Ader et al., 2012; Beeler et al., 2013) are discussed in the context of the observations. Both of these models are found to be lacking. Moreover, the SAF LFE data are clustered, and following a qualitative clustering analysis and formal declustering of the catalog (section 2.1), we find that the catalog is dominated by cluster durations that are too short for slip modulation on that time scale. In addition, the cluster recurrence interval is much longer than the semidiurnal period. With these temporal properties, the clusters appear to be triggered. Using a conceptual model of truly triggered occurrence, section 3, we evaluate the implications for fault properties. Since friction models imply dilatancy (Brace et al., 1966; Dieterich, 1979), experimentally observed dilatancy is described and the standard constitutive model of frictional dilatancy (Segall & Rice, 1995) is incorporated into the triggering model in section 3.1. Then, the data are used to constrain friction, dilatancy, and effective normal stress in the model, sections 3.2, 3.3, and 3.4. Finally, section 4 expands briefly on the implications and section 5 on known limitations of our study, and some suggested remedies.

1.1. Models of earthquakes and the tides

Among the large number of models of ETS processes (e.g., Ben-Zion, 2012; Hawthorne & Rubin, 2013; Hayman & Lavier, 2013; Liu & Rice, 2007; Segall et al., 2010; Skarbek et al., 2012, 2014) we limit our focus to those that directly address the correlation between the tides and low-frequency earthquake or tremor rates, and of those models only ones that can explain the details of the correlation. Due to the narrow scope of the observations under consideration, necessarily, we evaluate only a fraction of possible models, and therefore, nearly all our conclusions are inherently model-dependent.

In response to the shear-stress tides the earthquake rate increases approximately by 75% above the background rate, whereas the normal-stress tides have no systematic effect on the LFE earthquake rate

(Figure 1). One interpretation of the lack of a substantial and systematic sensitivity of earthquakes to normal stress is a ductile rheology with failure strength independent of pressure. However, a ductile rheology is not consistent with the presumed recurring episodic slip and repeating earthquake occurrence, most easily interpreted as brittle deformation. Two alternatives to ductile deformation have been suggested; the simplest, developed in reference to these SAF LFEs is that the fault failure strength is pressure dependent but with a very low friction coefficient (Thomas et al., 2012). Since the normal tides are more than 10 times larger the shear tides and have no coherent effect, this requires that the friction coefficient is much less than 0.1. Strictly, there are no laboratory measurements of sliding friction on geologic materials that have such low values and for the time being, we dismiss this possibility, returning to it later in section 4. An alternative was suggested by Hawthorne and Rubin (2010) in the context of triggered slip in Cascadia. They proposed that weak or absent correlation with the normal stress component of the tides can be explained by allowing the fault zone to be undergoing frictional sliding, at any absolute strength level, while the pore pressure within the fault is incompletely drained. So long as the fault zone has a high poroelastic coupling of stress to fluid pressure (a Skempton-like coefficient of ~1), as is expected at low effective normal stress, tidal changes in normal stress are opposed by changes in pore fluid pressure, the effective normal stress remains nearly constant, and expected changes in shear resistance or in slip rate due to the normal stress tides are diminished.

There are two classes of laboratory-based pressure-dependent models that have been used to explain the correlation between the tides and earthquake occurrence (Dieterich, 1987; Perfettini & Schmittbuhl, 2001), so in considering models of deep slip, we follow Hawthorne and Rubin's suggestion and assume that slip is frictional and allow that pore pressure is potentially undrained. Most relevant to seismic hazard are earthquake triggering models that were developed for seismicity in the upper part of the crust. In this brittle region, the fault is typically assumed to be effectively locked prior to failure. The onset of earthquake occurrence results from elastic stress transfer due to loading from plate motion outside the region of interest (tectonic loading) and from the tides, imposed as a body force in the model (see Appendix A). The modeled onset of slip depends on the stress level, resulting in an occurrence rate that reflects the characteristics of the tectonic loading and the influence of the tides. In the shallow crust there is generally a weak relation between the tides and natural earthquake occurrence (Métivier et al., 2009), and the majority of the moment release is thought to be seismic.

Appropriate for these conditions, triggering models descend from calculations with rate and state friction by Dieterich (1987), based on his room temperature experiments on initially bare quartzofeldspathic rocks and in later implementations from experimental studies by Lockner and Beeler (1999) and Savage and Marone (2007). The Dieterich (1987) model was developed for application to triggered seismic slip, in regions where such slip is the majority of the moment release. However, such observational restrictions on slip rate might not apply in the deep crust of our immediate interest. For instance, Hawthorne and Rubin (2010) show in Cascadia that deep slow events appear to be triggered, at depths where the majority of the strain release is aseismic rather than seismic. Similar to Hawthorne and Rubin (2010) our application of triggering models will be to slow slip.

The other class of models (Perfettini & Schmittbuhl, 2001) is specific to earthquake occurrence in regions where the predominant strain release mechanism is aseismic slip and the seismic moment is a small fraction of the total energy release (Nadeau & Johnson, 1998; Shelly et al., 2007). Accordingly, it is the surrounding slipping fault that provides the majority of the stress loading to the small areas of earthquake initiation. If the slip rate in the surrounding region is stress sensitive, then the tides modulate that rate and the earthquake occurrence rate reflects that modulation (Ader et al., 2012; Beeler et al., 2013; Hawthorne & Rubin, 2013; Perfettini & Schmittbuhl, 2001). Models of this second type are more consistent with the prevailing view of deep tectonic tremor and low-frequency earthquakes in that they are driven by slip of the immediately surrounding fault (Shelly et al., 2007), and indeed the Ader et al. (2012) and Beeler et al. (2013) models were developed to explain the strong correlation between NVT/LFEs and the tides using the assumption of slip loading as a starting point.

However, their assumption of slip loading does not preclude the possibility that the tidal correlation is due to triggered transient aseismic slip events rather than continuously modulated aseismic slip or to both. For example, again, since Hawthorne and Rubin (2010) showed that the onsets of deep slip episodes in Cascadia (e.g., Dragert et al., 2001) correlate with the tides, any seismic activity associated with that initial triggered slip is also triggered. Furthermore, in the context of slip loading, triggering and modulation are not mutually exclusive, and if slip is episodic with durations much longer than the tidal period, as is well known to be the case in Cascadia (e.g., Lambert et al., 2009), triggered slip may also be modulated by the tides (Hawthorne & Rubin, 2010) and the seismicity rates can show aspects of both.

In any case, so long as there are resolvable earthquake rate changes in response to known tidal stresses, the correlation might be used to determine the fault rheology, fault hydraulic properties, and potentially, the ambient effective stress levels in the source region (e.g., Hawthorne & Rubin, 2010; Thomas et al., 2012). As these determinations are necessarily model dependent, in this study, we address which model within these two classes, triggered or modulated slip, may be most appropriate and infer associated rheological parameters and conditions on the SAF.

2. Tidal Modulation of Fault Slip

Slip modulation models assume that an LFE is a brittle patch on a fault plane that is elsewhere and otherwise slipping aseismically (Bufe et al., 1977; Nadeau & Johnson, 1998; Perfettini & Avouac, 2004; Shelly et al., 2007) and that the LFE source itself is sufficiently small and obeys a threshold failure criteria such that occurrence is a passive meter of the rate of fault slip (Beeler et al., 2013)

$$\frac{V}{V_L} = \frac{R}{R_L} = \frac{N_{\text{obs}}}{N_{\text{exp}}}. \tag{1}$$

Here V and R are the slip and seismicity rates, respectively, and V_L and R_L are reference values of slip and seismicity rate, taken throughout as being associated with the plate motion rate on the SAF, $V_L \approx 0.001$ μm/s. As implied by (1), the normalized histogram of occurrence shown in Figure 1 can equivalently be expressed as a plot of the normalized fault slip rate, and the fault patches that produce seismicity have an occurrence rate that directly reflects the rheological properties of the surrounding fault. In both published models (Ader et al., 2012; Beeler et al., 2013) the fault has rate strengthening friction but the details differ considerably. Rate strengthening friction has the form

$$\tau = \sigma_e\left(\mu_0 + a\ln\frac{V}{V_0} + b\ln\frac{\theta V_0}{d_c}\right), \tag{2}$$

(Dieterich, 1979; Ruina, 1983), where a and b are small relative to the nominal friction coefficient μ_0, θ is the state variable of Ruina (1983) with steady state value $\theta_{ss} = V/d_c$, d_c is the state variable weakening distance, V_0 is a reference velocity, and $a > b$ (rate strengthening). For the Ader et al. (2012) model the fault is loaded elastically and there are four fault-controlled tidal response regimes that are separated by three characteristic time scales, defined by the relative contributions of the state variable to fault strength over the tidal period of interest and the onset of elastic interactions. The Beeler et al. (2013) model is much simpler; elastic interactions are ignored and the fault is purely rate strengthening (no state variable) and therefore has a single response regime where the fault always slides at steady state. To determine which model is most appropriate we first consider which of the Ader et al. (2012) regimes applies to the SAF LFEs. The response regimes in Ader et al. (2012) are, in order of lowest to highest period, as follows: instantaneous, state-influenced, steady state, and elasticity-dominated. The boundary between the instantaneous and state-influenced regimes is proportional to the steady state value of the state variable, $2\pi d_c/V_L$. Using a lab value of 200 μm for fault gouge for d_c (Ader et al., 2012), Figure 2 shows a recalculation of modulation for a wide range of tidal periods using the conditions of Ader et al. (2012) case #2. The daily and fortnightly tides are shown for reference and suggest that the dominant tidal response is in the instantaneous regime. The loading rate in Ader et al. (2012) (0.00063 μm/s) is somewhat lower than on the SAF, where, for the same choice of d_c, the regime boundary is at 1.26×10^6 s. This is still much higher than the semidiurnal tidal period that most strongly influences LFE rates on the SAF, requiring that the LFEs of interest are in the instantaneous regime.

The Ader et al. (2012) instantaneous response regime is essentially the same as that of the simpler Beeler et al. (2013) model, but, due to different assumptions, the derived amplitude of the slip rate responses can differ substantially: in Ader et al. (2012) the rate and state equations have been linearized resulting in $V/V_L = 1 + \Delta\tau/(a\sigma_e)$, while in Beeler et al. (2013), elastic loading is ignored, as if the tectonic loading were

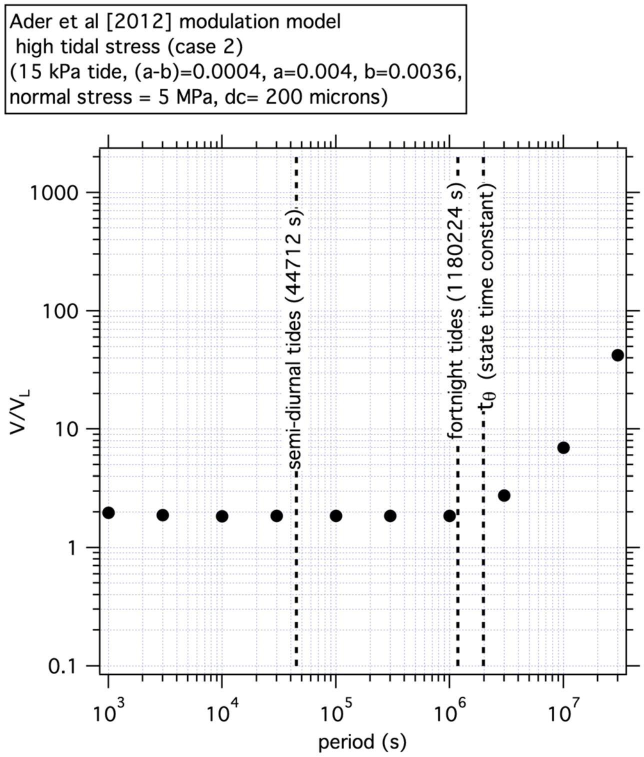

Figure 2. Tidal response regimes in a rate and state friction slip modulation model. Recalculation of Ader et al. (2012) case 2. The parameters used in the simulation are $\Delta\tau$ = 15 kPa, V_L = 0.02 m/yr, mean normal stress σ_n = 5 MPa, $k/\sigma n$ = 0.002/m, μ_0 = 0.7, a = 0.004, b = 0.0036, and d_c = 0.2 mm. The simulations are plotted as the velocity ratio V/V_L versus period T. The vertical dashed lines show t_θ, the fortnightly tide, and the semidiurnal tide.

infinitely compliant, resulting in $V/V_L = \exp[\Delta\tau/(a\sigma_e)]$. While the results are identical when the tidal amplitude $\Delta\tau$ is small relative to $a\sigma_e$ (i.e., when $\exp x \approx 1 + x$), for application at very low effective stress on the SAF (e.g., Thomas et al., 2012), this may not be the case and the nonlinearity of the earthquake rates may be important. Indeed, the SAF observations show strong evidence of nonlinearity (Thomas et al., 2009; 2012; Figure 1), as do LFE and tremor rates elsewhere (Houston, 2015; Ide & Tanaka, 2014). Similarly, while Ader et al. (2012) suggest that elastic stress transfer is unimportant for slip in the instantaneous regime, they do not consider low effective stress conditions where elasticity may influence the tidal response, and generally for application to the SAF and elsewhere, numerical simulations rather than either of the published, approximate models are recommended.

More important for our application to the SAF is whether a modulation model is appropriate for the observations. There is inconsistency between the assumption of modulated slip and the observation that the LFE occurrence is episodic (clustered in time) (Shelly, 2010; Thomas et al., 2012) (Figure 3), as follows, using Figure 3 as an example. For this family (#5 Shelly & Hardebeck, 2010), on the time scale of the whole catalog (~11 years), the event rate is apparently smoothly varying, which is not inconsistent with the idea that the rate might be modulated by the tide. This is an example of a “continuous” LFE family (Shelly, 2010; Shelly & Johnson, 2011; Thomas et al., 2012). However, on a much shorter time scale (inset), rather than smooth, occurrence is clustered, with ~8 events in each cluster and an average cluster recurrence interval of 0.0092 years (Table 1). To determine whether these clusters or episodes in the entire catalog are consistent with modulation during the cluster or with triggering requires processing the occurrences for recurrence interval and duration. In the following section we first develop a catalog processing routine. We focus only on the continuous families for a number of reasons. The continuous families are the large majority, 55, of the 88 families (Table 1), and the continuous families have more events per family than the “episodic” families (Shelly, 2010). In addition, clustering is similar among the continuous families. For these reasons we believe that the correlation of earthquake occurrence with the tides in the whole catalog is dominated by the behavior of the continuous families. As we will show, this is borne out by our analysis. The continuous families can be distinguished from episodic families in a number of ways, for example, as defined by the Shelly and Johnson (2011) MFD75 parameter. Here we define the continuous families as those that show clustering on a single time scale, whereas episodic families are clustered on two time scales.

2.1. Catalog Processing

We developed a simple catalog processing procedure to define all the individual episodes, episode recurrence times, episode durations, and number of LFEs per episode. To characterize a LFE family catalog, the catalog is divided into two sets of events, LFEs that occur during episodes and those that occur in the interepisode period. The division is done in two steps. First, interevent times are calculated for all LFEs—the interevent time is the time since the previous LFE in the family. The interevent time is also the reciprocal of the instantaneous occurrence rate of the family. Interevent times or occurrence rates are plotted on log scale versus time within the catalog (Figure 4a); in this report the occurrence rate is used. The division in this figure is defined by the horizontal region in the center of the plot where there are few events; this region of depleted occurrence lies between 1/average episode recurrence interval and 1/average interevent times during episodes. A naive but effective procedure for objectively determining the location of this break is to sort the log of the reciprocal of the interevent times and to take the largest value of the difference between consecutive values (Figure 4b). In this example the break in the catalog is at 1.44 (in log (1/d)). Episodes are defined by two or more consecutive occurrences with interevent times that are shorter than the break. This

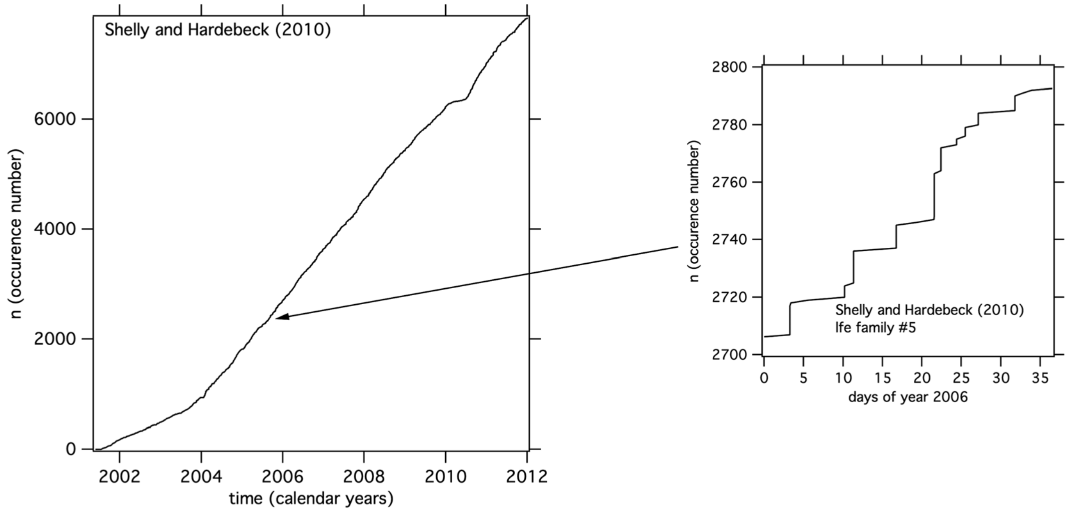

Figure 3. Earthquake occurrence for an example LFE family catalog, a “continuous” family, #5 (Shelly & Hardebeck, 2010). The inset shows the episodic nature of occurrence on an expanded scale spanning 36.5 days.

procedure is followed for all 55 continuous families defining catalogs of episode duration, number of events per episode, episode seismicity rate, and episode recurrence interval. The averages of each of those quantities are calculated for each family in Table 1.

To illustrate clear constraints on models of tidal correlation from this analysis, note the relation of the episode duration and recurrence interval to the daily tidal period for the example family #5 (Figure 4c). The semidiurnal period is more than 2 orders of magnitude longer than the average episode duration of 302 s, meaning that to first order, all of the LFEs in each episode occur at the same time relative to the tidal period. This indicates that no significant modulation of slip is possible during episodes. The average recurrence interval in this family is 3.4 days, intermediate between the semidiurnal and fortnightly tides. We extend this idea to the behavior of all the continuous families by constructing a “declustered” catalog. The catalog consists of the occurrence time of the first LFE in each episode, representing the episode onset time, for all the continuous families relative to the tidal stress (Figure 5). To avoid possible influences of the 2004 Parkfield earthquake (e.g., Shelly, 2017) we undertake the analysis from 2005.5 (07/02/05) to the end of the catalog (1/4/2012). As shown in Figure 5 there is little difference between the tidal correlation of the whole LFE catalog (2001–2012) and the post Parkfield subset (2005.5–2012). Furthermore, relative to the shear stress tides (Figure 5a), the episode onsets (solid black symbols) follow a similar trend as the entire LFE catalog (gray symbols), while relative to the normal stress tides, the episode onsets (Figure 5b solid black symbols) are similar to the entire LFE catalog (gray symbols) and show no systematic relationship to the tidal stress. These observations confirm that the LFE catalog is dominated by the behavior of continuous families, and on the time scale of the episodes, the correlation does not arise from modulation of slip by the tides. The latter result has been discussed in a more general context by Thomas et al. (2017), who consider in detail the assumption underlying our analysis, that LFE rates are proportional to the slip rate of the fault. Thomas et al. (2017) conclude that for continuous families, during clusters, LFE occurrence rates are not proportional to the fault slip rate. Consequently, these short duration bursts cannot be interpreted as slow slip events but instead represent some kind of compound rupture driven to failure by surrounding slow slip. That surrounding slow slip, if variable, for instance due to the tidal stress, varies at longer time scales than the continuous family cluster duration (Thomas et al., 2017).

The rate of occurrence of the episode onsets in the declustered catalog is much less than an event per tidal cycle; for example, for family #5, the rate is 0.15 episode onsets per tidal cycle. Accordingly, there is no resolution of modulation on the time scale of a single tidal period and the onsets have the appearance of being triggered by the tides, a property we refer to in the remainder of this paper as “apparent” triggering. In the context of specific triggering and modulation models, this behavior could be due to either. For a

Table 1
Continuous Family Episode Catalog and Properties

Family	N	N_e	$\hat{R}_t = N/T$ (1/yr)	$\hat{t}_d$ (year)	$\hat{R}_e$ (1/yr)	$\hat{R}_e/\hat{R}_t$	$\hat{t}_r$ (year)	Latitude (deg)	Longitude (deg)	Depth (km)
1	2,264	344	348.9	5.07e−6	1.75e+6	5,014.3	0.0186	35.44	−120.01	23.5
2	2,085	322	321.3	6.42e−6	1.51e+6	4,698.1	0.0200	35.505	−120.115	29
3	3,085	458	475.0	4.87e−6	1.74e+6	3,671.5	0.0141	35.53	−120.075	28.5
4	3,962	499	608.8	1.44e−5	9.62e+5	1,580.8	0.0130	35.54	−120.11	26.5
5	5,583	701	857.9	9.58e−6	1.52e+6	1,771.5	0.0093	35.575	−120.11	26.75
6	4,856	630	746.6	7.19e−6	1.66e+6	2,218.0	0.0103	35.61	−120.175	26
7	3,101	374	476.9	9.56e−6	1.29e+6	2,705.0	0.0174	35.62	−120.185	25.75
8	5,300	731	814.9	9.24e−6	1.51e+6	1,856.8	0.0089	35.625	−120.2	26.25
9	10,379	755	1,596.2	1.13e−5	1.64e+6	1,029.9	0.0086	35.625	−120.15	28.75
10	6,820	997	1,048.6	5.52e−6	1.85e+6	1,765.5	0.0065	35.63	−120.19	25
11	4,193	598	644.8	9.40e−6	1.12e+6	1,737.2	0.0109	35.635	−120.15	28.5
12	4,378	616	673.3	8.50e−6	1.29e+6	1,916.5	0.0106	35.635	−120.205	24.5
13	2,334	379	359.0	6.76e−6	1.30e+6	3,612.1	0.0171	35.64	−120.22	27
14	3,070	466	471.8	3.25e−6	2.24e+6	4,754.0	0.0140	35.64	−120.14	26.5
15	3,535	562	544.5	2.86e−6	2.56e+6	4,698.6	0.0115	35.66	−120.215	22.75
20	4,367	733	671.3	3.54e−6	2.21e+6	3,286.0	0.0089	35.675	−120.265	21
21	4,785	781	735.8	6.97e−6	2.29e+6	3,113.9	0.0083	35.68	−120.24	24
29	3,182	560	490.5	2.00e−6	3.39e+6	6,902.6	0.0115	35.72	−120.28	22.25
33	5,765	930	890.3	3.39e−6	2.81e+6	3,154.2	0.0070	35.745	−120.32	19.75
37	1,970	288	303.7	5.30e−6	2.65e+6	8,734.1	0.0225	35.78	−120.325	23.5
40	3,781	614	583.0	2.96e−6	2.92e+6	5,011.6	0.0105	35.79	−120.325	23.75
41	5,817	587	896.8	1.70e−5	1.18e+6	1,311.0	0.0110	35.79	−120.34	25
44	3,009	453	462.6	3.65e−6	2.39e+6	5,160.2	0.0143	35.845	−120.427	19.5
45	3,374	529	518.6	4.22e−6	2.09e+6	4,030.5	0.0123	35.852	−120.362	24.25
46	6,969	848	1,071.5	4.04e−6	2.41e+6	2,246.2	0.0077	35.852	−120.36	24.62
47	3,102	489	476.8	7.80e−6	1.36e+6	2,844.6	0.0133	35.875	−120.39	21
48	2,695	417	414.3	6.81e−6	1.22e+6	2,939.3	0.0156	35.877	−120.395	23.62
49	4,638	658	713.8	7.78e−6	1.84e+6	2,577.0	0.0099	35.975	−120.515	18.75
50	3,084	484	474.0	8.04e−6	1.15e+6	2,427.4	0.0134	35.98	−120.515	16.25
51	6,337	902	974.3	1.05e−5	1.01e+6	1,035.3	0.0072	35.98	−120.515	16.75
52	7,817	961	1,201.5	7.48e−6	1.49e+6	1,241.1	0.0068	35.98	−120.525	21.25
54	5,931	671	912.9	6.33e−6	1.91e+6	2,092.4	0.0097	36.005	−120.575	17.5
57	6,495	721	999.7	1.07e−5	1.40e+6	1,398.0	0.0090	36.01	−120.545	21.5
60	10,049	788	1,546.8	2.55e−5	1.01e+6	655.3	0.0082	36.055	−120.585	23
62	14,687	1053	2,257.8	2.29e−5	1.20e+6	532.1	0.0062	36.08	−120.655	19.25
63	7,729	752	1,188.2	1.19e−5	1.75e+6	1,475.2	0.0086	36.085	−120.615	23
66	9,782	654	1,503.8	1.43e−5	1.66e+6	1,102.1	0.0099	36.1	−120.65	19
67	5,385	745	828.9	9.59e−6	1.63e+6	1,971.9	0.0087	36.12	−120.645	23
68	6,067	778	933.9	5.84e−6	1.97e+6	2,112.0	0.0083	36.12	−120.64	21.5
69	4,645	513	714.1	3.11e−5	8.51e+5	1,191.8	0.0127	36.12	−120.635	25.75
70	4,818	618	740.9	5.98e−6	2.06e+6	2,785.7	0.0105	36.12	−120.64	25.25
73	4,797	677	738.4	4.43e−6	2.27e+6	3,070.9	0.0096	36.135	−120.69	19
74	7,149	773	1,100.2	1.18e−5	1.39e+6	1,265.8	0.0084	36.14	−120.665	21
75	7,093	884	1,090.8	4.22e−6	2.54e+6	2,324.6	0.0073	36.14	−120.67	25.25
77	7,625	848	1,172.6	5.60e−6	2.33e+6	1,984.8	0.0077	36.175	−120.725	26.25
78	2,895	597	444.9	1.21e−6	4.16e+6	9,350.4	0.0109	36.18	−120.735	26
79	6,971	877	1,072.0	5.12e−6	2.44e+6	2,272.5	0.0074	36.2	−120.745	25.75
80	13,473	997	2,071.6	2.21e−5	1.29e+6	620.3	0.0065	36.21	−120.72	22.5
81	11,211	778	1,725.3	1.47e−5	1.78e+6	1,031.6	0.0083	36.22	−120.77	24.75
82	11,099	1,191	1,706.9	5.82e−6	2.13e+6	1,247.4	0.0055	36.23	−120.79	27.25
83	8,611	656	1,324.3	2.09e−5	8.75e+5	660.9	0.0099	36.258	−120.805	24.75
84	7,356	895	1,131.5	1.00e−5	1.84e+6	1,623.6	0.0073	36.28	−120.835	23.75
85	8,524	1,064	1,311.4	4.68e−6	2.28e+6	1,738.5	0.0061	36.29	−120.83	24.62
86	5,411	715	831.9	5.81e−6	1.68e+6	2,019.0	0.0091	36.32	−120.925	23.5
87	13,075	1,056	2,012.0	7.56e−6	2.03e+6	1,008.7	0.0061	36.435	−121.08	23.5

Note. Latitude, longitude, and depth from Shelly and Hardebeck (2010). N—number of LFEs, N_e—number of episodes, $\hat{R}_t$—average seismicity rate, $\hat{t}_d$—episode duration, $\hat{R}_e$—average seismicity rate during episodes, $\hat{R}_e/\hat{R}_t$—seismicity rate ratio, and $\hat{t}_r$—episode recurrence interval.

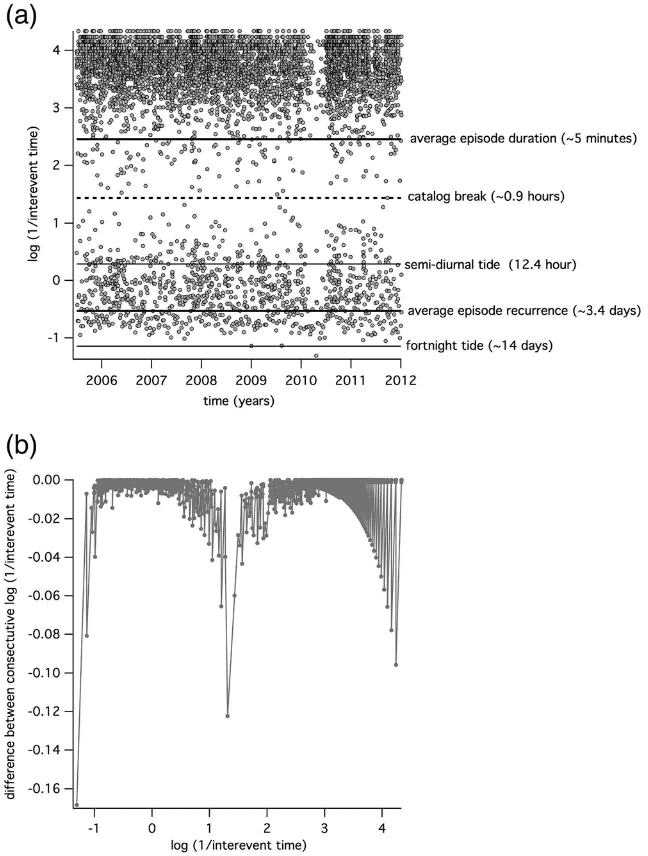

Figure 4. Temporal properties of a continuous LFE family catalog, #5 of Shelly and Hardebeck (2010). Logarithm of instantaneous seismicity rate (1/interevent time with time in days) versus time in years between 2005.5 and 2012. Also shown are the average episode duration, episode recurrence interval, the semidiurnal tidal period (44,712 s), the fortnight (1,180,224 s), and the break in the catalog used to define the episodes (see text for discussion). (b) Sorted logarithm of seismicity rate (horizontal axis) and the gap between successive rates (vertical axis). Seismicity rate is in events/d. The local minimum at 1.44 on the horizontal axis corresponds to the center of the horizontal low density band in Figure 4a. This value is used to divide the catalog in Figure 4a into events within episodes, log values above 1.44, and those that are between episodes, values below.

triggering model the onsets might represent triggered deformation within the region containing clusters. Since the duration of episodes is long relative to earthquake risetimes, this would be a triggered creep model with each episode onset being used as a proxy for the onset of detectable slip (see Thomas et al. (2017) for detailed discussion of the temporal resolution of LFE families). For modulation, the model would be no different than described in the prior studies of Ader et al. (2012) and Beeler et al. (2013), except the region containing episodes would have to be spatially large enough or the stress drop associated with failure be large enough that reloading to failure takes multiple tidal cycles. Because modulation models are well represented in the literature and have been applied previously to LFEs (Royer et al., 2015) and nonvolcanic tremor (Yabe et al., 2015), we focus on constraints from the unexplored possibility that these episodes may be truly triggered slip events.

3. Tidal Triggering of Slip

Given the lack of systematic normal stress dependence and discounting the possibility that the friction coefficient is much less that 0.1, interpreting the observations as due to triggered frictional slip requires the fault to be incompletely drained over the tidal period. Appendix A considers poroelasticity and triggered slip over a range fluid diffusivities from undrained to drained conditions, relative to the daily tides. In these calculations, for undrained conditions, the earthquake rate is in-phase with the tidal shear stress, but as the diffusivity increases, the normal tides begin to influence the earthquake rate, and necessarily, the in-phase relationship with the shear tides is lost. At drained conditions the effect of normal tides on fault slip is fully manifest. The observed SAF seismicity rate relative to the daily tides (Figure 1), when interpreted in the context of these calculations, places a qualitative bound on the diffusivity in the source region to be less than about 1×10^{-6}/s. While these calculations are somewhat involved and would seem to be highly model-dependent, the essential constraints on the diffusivity come from the data: the observed lack of sensitivity to the normal tides (Figure 1b), the in-phase with shear tides (Figure 1a), and the semidiurnal tidal period t_p of 44,712 s. These require that the fault is not drained at diffusivities of $1/t_p$ or ~2×10^{-5}/s. Thus, the diffusivity is on the order of or smaller than the reciprocal of 10 times the tidal period, and the inference made in Appendix A is likely to be independent of the particular triggering model.

Requiring nondrained fault slip puts additional constraints on the fault rheology because frictional deformation is fundamentally dilatant (Brace et al., 1966). Changes in pore volume due to dilatancy or compaction will change the effective stress inside an incompletely drained fault zone. For example, in friction experiments, shear zone porosity varies systematically with slip rate (Marone et al., 1990; Morrow & Byerlee, 1989). Figure 6 shows this effect in saturated quartz gouge at room temperature and 100 MPa normal stress from Marone et al. (1990). On a rate-weakening fault with this property and with incompletely drained fluid pressure, slip acceleration produces dilatancy and an increase in the effective normal stress, slowing, and potentially stabilizing fault slip (Segall & Rice, 1995), as described in detail as follows.

3.1. Dilatancy Rate Dependence

Rate-dependent dilatancy provides the basis for a number of theoretical and numerical studies of crustal-scale faulting (Segall & Rice, 1995) and deep slow slip (Liu & Rubin, 2010; Segall et al., 2010; Segall & Bradley, 2012), using the constitutive equations developed by Segall and Rice (1995). In these faulting studies the modeled slip velocities range from substantially below the plate rate up to seismic rates, and the depth

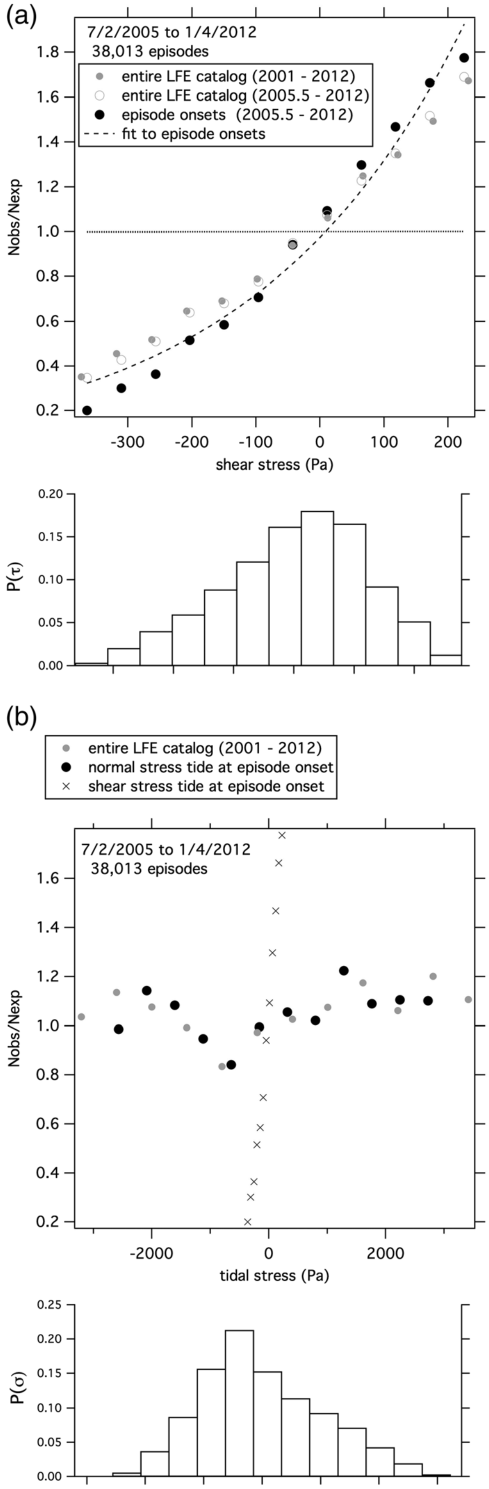

Figure 5. Relation between LFE occurrence and the tidal stress for continuous family episodes, ~38,013 episode onsets from 55 LFE families between 07/2005 and 01/2012. (a) Upper plot. The left vertical axis is the observed number of episode onsets normalized by the expected number. The horizontal axis is the tidal shear stress. A fit to the form (9) (dashed) has $c = 0.98$ and $A_{\text{fit}} = 330$ Pa. Shown for reference is $N_{\text{obs}}/N_{\text{exp}}$ for the entire LFE catalog (01/01/2001–01/04/2012) from Figure 1a and the values for the catalog from 07/02/2005 to 01/04/2012. The dotted nearly horizontal line represents that the predicted event numbers were the earthquake rate controlled by steady state dilatancy hardening in a quartz gouge using room temperature dilatancy measurements (see text). The lower plot shows the probability density of the tidal shear stress associated with the episodes. (b) Same as Figure 5a for the tides resolved as fault normal stress. Shown for reference are $N_{\text{obs}}/N_{\text{exp}}$ for the entire LFE catalog (small gray symbols) from Figure 1b and the shear stress data from part Figure 5a (x's). The lower plot shows the probability density of the tidal normal stress associated with the episodes.

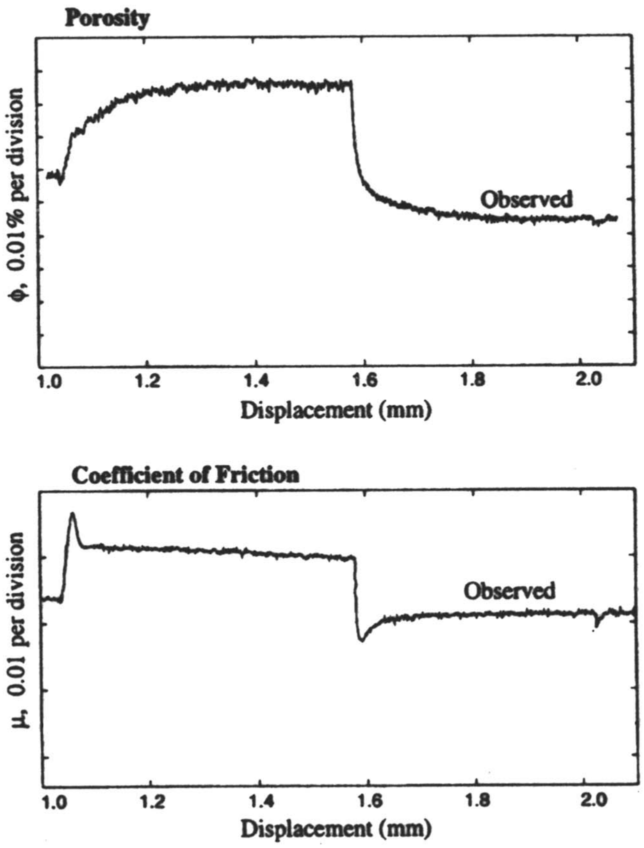

Figure 6. Rate-dependent dilatancy and friction in saturated quartz gouge at room temperature and 100 MPa normal stress from the seminal study of Marone et al. (1990). (a) Fault zone evolves following a change in slip rate; in this case, there are two rate changes. In response to the first order of magnitude step increase in slip rate, the fault becomes more dilated, and then compacts following the subsequent slip rate decrease. The data shown have had a positive linear (compaction) trend removed. (b) Friction changes rapidly when slip rate is changed following the two stage response of Dieterich (1979), in this case resulting in a net increase in steady state friction following the increase in slip rate, then a decrease in steady state friction when the slip rate is returned to the origin rate (rate strengthening). The figure is reproduced from Segall and Rice (1995).

varying effective normal stresses range from near zero near the surface to those expected at the base of the lithosphere in strike-slip and subduction zone settings. In the subduction zone models, it is this effective “dilatancy rate strengthening” that limits slip to subseismic rates while producing quasiperiodic occurrence (Liu & Rubin, 2010; Segall et al., 2010; Segall & Bradley, 2012). Collectively, these studies require that rate-dependent dilatancy occurs throughout the crust independent of slip speed, normal stress, and mineral composition. The experiments upon which this is based are limited to room temperature quartz and granitic faults and gouges (e.g., Morrow & Byerlee, 1989; Marone et al., 1990), at a limited range of normal stress and slip speed.

To determine the expected contributions from dilatancy we allow the fault to slip over the range of conditions between drained and undrained. Fault strength is the product of a friction coefficient, μ, and the effective normal stress

$$\tau = \mu(\sigma_n - p), \tag{3}$$

where σ_n is the applied fault normal stress and p is pore fluid pressure. The steady state rate-dependent dilatancy is assumed to follow the laboratory-based constitutive relation proposed by Segall and Rice (1995),

$$\phi_{ss} = \phi_0 + \varepsilon \ln \frac{V}{V_0}, \tag{4}$$

where ϕ is porosity of the shear zone, the ratio of the pore volume to the total volume, and V_0 and ϕ_0 are arbitrary reference values of slip velocity and porosity. ε is the experimentally measured rate dependence of porosity, $\varepsilon = d\phi/d \ln V$. The rate-dependent porosity is thought to result from competition between time-dependent compaction and shear-induced dilatancy. Equation (4) strictly describes the steady state response of dilatancy and therefore dictates only the maximum amplitude of the pore pressure response to dilatancy (see section 3.4 below where the nonsteady state behavior is included). At drained conditions, rate-dependent dilatancy (4) makes no contribution to the fault strength (3).

More generally, following Walder and Nur (1984) and Segall and Rice (1995), a fluid mass balance requires that the rate of change of fluid mass per unit volume, m, depends on the sum of terms representing the rate of change of the porosity and that of the pore fluid pressure

$$\frac{dm}{dt} = \rho_f \left(\phi\left(\beta_f + \beta_\phi\right) \frac{dp}{dt} + \frac{d\phi}{dt} \right). \tag{5a}$$

where ρ_f is fluid density, $\beta_f = (1/\rho)(d\rho/dp)$ is the fluid compressibility, and $\beta_\phi = (1/\phi)(d\phi/dp)$ is the pore compressibility. Undrained conditions, that is, $dm/dt = 0$ in (5a), define the relation between dilatancy and pore pressure to be

$$\frac{dp}{dt} = -\frac{1}{\phi\left(\beta_f + \beta_\phi\right)} \frac{d\phi}{dt} \tag{5b}$$

(Segall & Rice, 1995), where they used the substitution $\beta = \phi(\beta_f + \beta_\phi)$ as the combined compressibility of the fluid and pores. Combining (5b) with the derivative of (4) (assuming $\phi = \phi_{ss}$) results in

$$\frac{dp}{dt} = -\frac{\varepsilon}{V\phi\left(\beta_f + \beta_\phi\right)} \frac{dV}{dt}. \tag{5c}$$

Equation (5c) is the undrained rate of pore pressure change associated with changes in slip rate that we use initially, keeping in mind that this is the amplitude of pore pressure response due to only the steady state dilatancy; subsequently, we will also examine the nonsteady state response. Accordingly, the material contribution of dilatancy to pore pressure change is manifest as the coefficient ε, the size of the porosity change, and throughout this study, ε is referred to as "the dilatancy coefficient."

Table 2
Parameters Used to Estimate the Expected Dilatancy Hardening Contribution to Friction

	Shallow (Hydrostatic)	Deep (Lithostatic)
Depth (km)	15	30
Temperature (°C)	380	620
Pore pressure (MPa)	150	840
β_f (1/MPa)	1.2×10^{-3}	3.2×10^{-4}
ϕ	0.01	0.1
β_ϕ (1/MPa)	1×10^{-2}	1×10^{-2}
μ_0	0.7	0.7
ε	1.7×10^{-4}	1.7×10^{-4}
$\varepsilon\mu_0$	1.2×10^{-4}	1.2×10^{-4}
β (1/kPa)	1.12×10^{-7}	1.03×10^{-6}
$\varepsilon\mu_0/\beta$ (MPa)	1.01	0.11
$\Delta\tau$ (MPa)	2.3×10^{-4}	2.3×10^{-4}

3.2. Steady State Dilatancy and State

Quasi-periodic slip requires recurring stress drop, most reasonably explained by rate weakening frictional slip with restrengthening in the interevent period (Dieterich, 1979). For steady state dilatancy and state, rate and state friction follows an equation of the form of (2), with $a\sigma_e$ augmented by the dilatancy contribution $\left(a\sigma_e + \frac{\varepsilon\mu_0}{\beta}\right)$ (Segall & Rice, 1995) and where $b\sigma_e > \left(a\sigma_e + \frac{\varepsilon\mu_0}{\beta}\right)$ (rate weakening). Previously published rate step tests to determine ε for quartzite results in $\varepsilon = 1.7 \times 10^{-4}$ (Table 3), the associated friction value, $\mu_0 = 0.7$ (Marone et al., 1990; Segall & Rice, 1995), and we assume crack-like as opposed to equant porosity $\beta_\phi = 1 \times 10^{-2}$/MPa for β_ϕ at all depths (Segall & Rice, 1995). To estimate the remaining unknown constants, ϕ, and β_f, we consider a range of possible temperature and stress conditions within the transition zone as estimated by Beeler et al. (2013), using a strike-slip faulting environment with an optimally oriented fault where the intermediate principal stress is the mean stress and the geotherm of Lachenbruch and Sass (1973). Temperatures range between 380 and 620°C in the region of LFEs and tremor between 15 and 30 km. The normal stresses for an optimally oriented fault in this depth range from 420 MPa at 15 km to 840 MPa at 30 km. Taking the least extreme stress condition to be associated with the lowest pore pressure (hydrostatic), $p = 150$ MPa, at 15 km, and most extreme stress condition to have lithostatic pore pressure $p = 840$ MPa at 30 km, results in a range of values of β_f from most compressible, 1×10^{-3}/MPa, for the shallow extreme to least compressible 3.2×10^{-4}/MPa for the deep extreme (Burnham et al., 1969). Allowing the steady state porosity to vary between 1 and 10% with the high (shallow) to low (deep) effective normal stresses, respectively, leads to $\varepsilon\mu_0/\beta = 0.12$ to 1.1 MPa. The smaller value is for the high pore pressure, high temperature, high porosity conditions (Table 2).

If we take these frictional properties inferred from room temperature measurements as appropriate for these depths, a minimum fluid pressure for nucleation of repeating slip can be inferred from the requirement that the steady state friction is rate weakening, namely,

$$\sigma_e \geq \frac{\varepsilon\mu_0}{\beta(b-a)}. \tag{6}$$

A low temperature value of $(b - a)$ for localized slip in quartz is 0.005 (Chester, 1995), yielding minimum values for effective normal stress in the range of 22 to 202 MPa. These are very high relative to the amplitude of tidal shear stress that produces the strong correlation with the tides and are inconsistent with a prevailing view that to produce strong correlation with the tides requires the ambient stress levels to approach the amplitude of the tide (Thomas et al., 2012), for instance, second-order relative to the tidal stress (Beeler et al., 2013). The disagreement may be an indication of inconsistency between the frictional properties measured in room temperature experiments on quartzofeldspathic rocks and those that may control earthquake occurrence in the deep crust, pending the results from our nonsteady state calculations to follow. Since smaller magnitude (more neutral) values of the rate dependence might be expected in the brittle ductile transition region (e.g., Ader et al., 2012) and because such values would raise the minimum effective stress in (6), qualitatively, the primary requirement of the tidal correlation on frictional properties would be to reduce the $\varepsilon\mu_0$ product relative to room temperature values. Moreover, the implied range of stress change due to dilatancy from the quartz experiments $\varepsilon\mu_0/\beta = 0.12$ to 1.1 MPa greatly exceeds the stress drops of natural slow slip events (e.g., Rubin, 2011), further implying fundamental differences in frictional properties between low temperature lab tests and at the elevated temperatures in the deep crust.

3.3. Steady State Dilatancy, Nonsteady State

While using low temperature friction parameters in (6) seems to provide effective stress that is too high to explain the tidal correlation, we take the result as an upper bound on effective stress for this triggering model. In this and the following section we make more complete estimates of the frictional properties and effective stress for tidal triggering on the SAF by allowing the friction parameters to deviate from the low-temperature measurements and for friction to deviate from steady state. In this section we assume that steady state dilatancy, equation (4), applies throughout earthquake nucleation and simulate fault slip with (5c) for pore fluid pressure, (3) for effective stress, and (2) for friction and assume that the effective normal stress in the absence of shear-induced dilatancy is constant. An evolution relationship for the state variable

$$\frac{d\theta}{dt} = -\frac{V\theta}{d_c}\ln\left(\frac{V\theta}{d_c}\right), \tag{7}$$

(Ruina, 1983) completes the friction constitutive equation (2). Shear loading consists of a nominal constant rate of stressing that represents tectonic loading and an oscillating stress representing the tides that is imposed as a body force,

$$\frac{d\tau}{dt} = k(V_L - V) + \frac{2\pi\Delta\tau}{t_p}\cos\left(\frac{2\pi t}{t_p}\right), \tag{8}$$

where we have represented the tidal shear stress as a simple sine function. k is the stiffness, $\Delta\tau$ is the amplitude of the tidal shear stress, t_p is the tidal period, and V_L is the loading velocity. The calculations follow the approach of Dieterich (1987) in spirit and consist of a population of N sources that are initially far from failure with identical frictional properties. The initial phase of the tidal stress for these sources is distributed uniformly over the tidal period t_p. When $\Delta\tau = 0$ the failure rate of the population, the seismicity rate, is constant at N/t_p. The friction parameters, fault properties, stresses, tides, and pore pressure were selected to match known conditions on the deep San Andreas (see caption to Figure 7) and to produce earthquake rates that are qualitatively consistent with the observations. Results are independent of the values of b and d_c in (2), and in all calculations, the peak earthquake rate coincides with the peak stress of the tide (cf., Beeler & Lockner, 2003); that is, the earthquake rate is in phase with the tidal stress as required by the observations. Simulated distributions of $N_{\text{obs}}/N_{\text{exp}}$ with respect to the tidal stress (Figure 7a) can be fit empirically with

$$\frac{N_{\text{obs}}}{N_{\text{exp}}} = c\exp\left(\frac{\Delta\tau}{A_{\text{fit}}}\right). \tag{9}$$

The preexponential constant c measures the offset of the exponential from $N_{\text{obs}}/N_{\text{exp}} = 1$ at $\Delta\tau = 0$, as in the example (Figure 7a) where $c = 0.68$. Fits with (9) to the results of our calculations yield values of c between 0.5 and 1 (Figures 7b and 7c). The values of A_{fit} scale with the sum $\left(a\sigma_e + \frac{\varepsilon\mu}{\beta}\right)$ as expected from the undrained analysis of Segall and Rice (1995) (Figures 7b and 7c). Figure 7b shows a suite of calculations over a range of effective normal stresses for the end-member case where the dilatancy coefficient $\varepsilon = 0$ such that the earthquake rate reflects the instantaneous rate dependence most directly. In those calculations $a = 0.007$ and the starting value of effective normal stress is varied between 0.03 and 0.07 MPa. Because there is no dilatancy, effective stress is constant throughout all the calculations. The dashed line is $A_{\text{fit}} = 0.7A$, where $A = \left(a\sigma_e + \frac{\varepsilon\mu}{\beta}\right)$ and indicates that the apparent rate dependence in (9) is somewhat smaller than the input values of the sum $\left(a\sigma_e + \frac{\varepsilon\mu}{\beta}\right)$. Figure 7c is a similar calculation where the input values of the rate dependence sum $\left(a\sigma_e + \frac{\varepsilon\mu}{\beta}\right)$ are the same as in Figure 7b but where $\varepsilon \neq 0$. This is accomplished by setting a to half the value used in the prior simulations, $a = 0.0035$, and as σ_e is varied from 0.03 to 0.07, ε is covaried from 1.5×10^{-7} to 3.5×10^{-7} such that $a\sigma_e = \varepsilon\mu/\beta$ in all simulations. Because the fault has nonzero ε, it dilates, raising the effective stress and porosity with slip such that, at failure, neither ϕ or σ_e are their starting values. Nonetheless, other than $\left(a\sigma_e + \frac{\varepsilon\mu}{\beta}\right)$ being systematically larger at failure, the simulations are no different than those in Figure 7b. Again in Figure 7b, $A_{\text{fit}} = 0.7A$ is shown as a dashed reference line.

3.4. Nonsteady state Dilatancy and State

Because there is known displacement evolution of dilatancy following a change in slip speed (Figure 6), the assumption of steady state in (4) may lead to an overestimate of the role of dilatancy hardening on earthquake rates. Better estimates may come from assuming an evolution relationship for porosity:

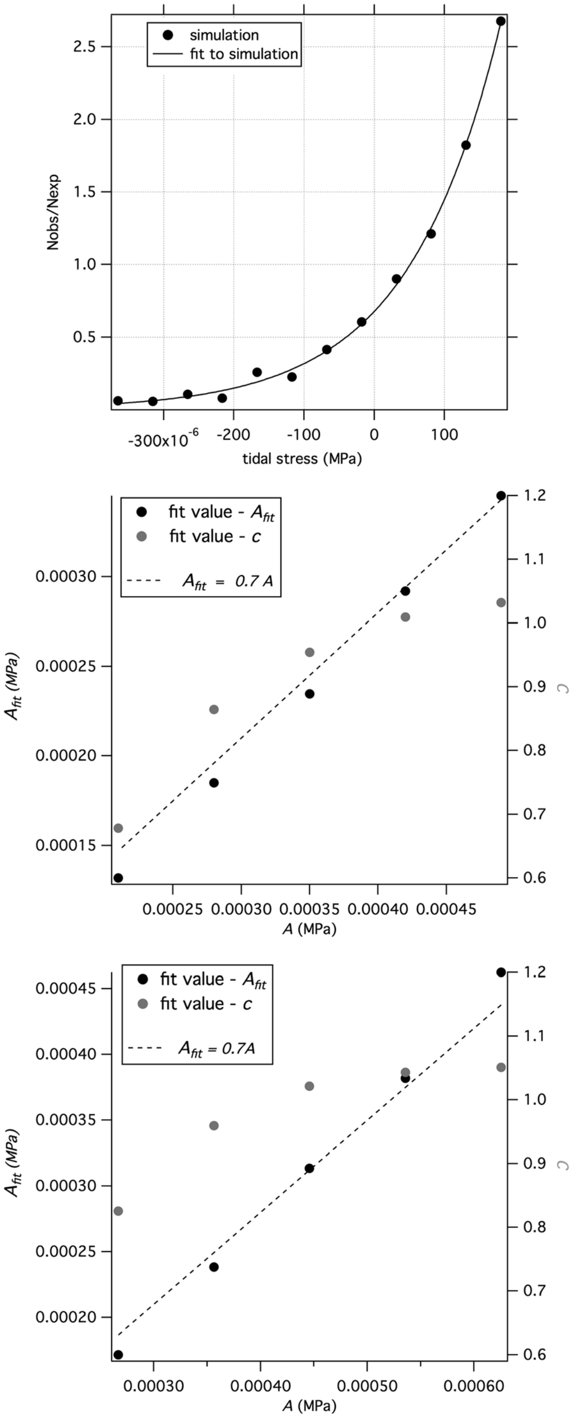

Figure 7. Simulations of triggered slip. (a) Example simulation in number of events versus tidal stress level for $\mu_0 = 0.7$, $a = 0.007$, $b = 0.015$, $d_c = 3\ \mu\text{m}$, $\beta_f + \beta_\phi = 0.1/\text{MPa}$, $\phi = 0.1$, $\varepsilon = 0$, $\sigma_e = 0.03$ MPa, $k = 6 \times 10^{-7}$ MPa/μm, $V_L = 0.001$ μm/s, $t_p = 44{,}712$ s, $\Delta\tau = 0.00023$ MPa, and $N = 500$. The solid symbols are the simulation; the line is fit to the simulation with equation (9), resulting in $A_{\text{fit}} = 0.00013$ MPa, $c = 0.68$. (b) Fit values of c and A_{fit} from a suite of simulations, with the same parameters as in Figure 7a except σ_e is varied from 0.03 to 0.07. Each simulation results in earthquake rates over the range of tidal stresses, as shown in Figure 7a. Each of those resulting histograms is then fit with the empirical earthquake rate equation (9). This figure shows the values of the two fitting parameters A_{fit} and c of equation (9), plotted against the value of the rate dependence used in the simulations, $a\sigma_e + \frac{\varepsilon\mu}{\beta}$. The solid symbols are the values, A_{fit} (left axis). Fit values of c are in gray (right axis). The dashed line is the result if the fit value is $A_{\text{fit}} = 0.7\left(a\sigma_e + \frac{\varepsilon\mu_0}{\beta}\right)$. (c) Fit values of c and A_{fit} from a suite of simulations with the same parameters as in Figure 7a, except $a = 0.0035$, and σ_e is varied from 0.03 to 0.07 and ε is covaried from 1.5×10^{-7} to 3.5×10^{-7} such that $a\sigma_e = \varepsilon\mu/\beta$ in all simulations.

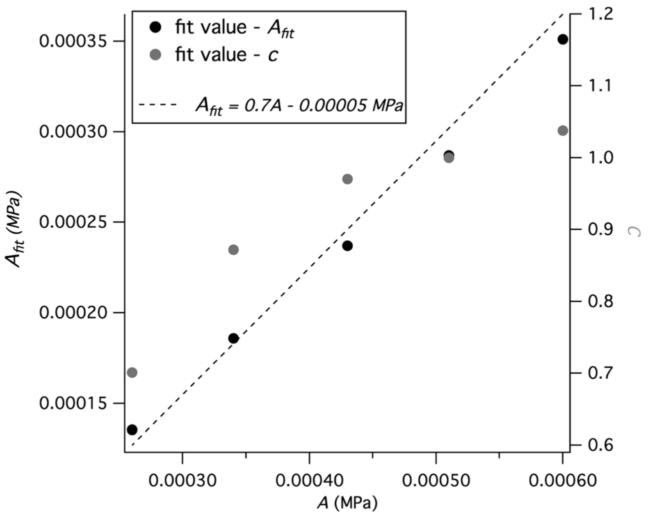

Figure 8. Simulations of triggered slip with nonsteady state dilatancy. Fit values of *c* and A_{fit} from a suite of simulations with the same parameters as in Figure 7c. The dashed reference line is the result if the fit value is $A_{\text{fit}} = 0.7\left(a\sigma_e + \frac{\varepsilon\mu_0}{\beta}\right)$ + 0.00005 MPa.

$$\frac{d\phi}{dt} = -\frac{V}{d_c}(\phi - \phi_{ss}) \tag{10a}$$

(Segall & Rice, 1995), when combined with the steady state relationship (4) results in

$$\frac{d\phi}{dt} = -\frac{V}{d_c}\left(\phi - \phi_0 - \varepsilon \ln\frac{V}{V_0}\right) \tag{10b}$$

We use (10b) in nonsteady state calculations. In these, the d_c controlling dilatancy evolution is assumed to be the same as that for friction in (7) (e.g., Beeler and Tullis, 1997), an assumption that has been used in simulations of slow slip (Liu & Rubin, 2010) but has not been verified experimentally. In addition, in our nonsteady state calculations, we allow the fault to be undrained at times substantially longer than the tidal period. Following Segall and Rice (1995) for 1-D diffusion normal to the fault, we equate the second spatial derivative of pore pressure in equation (5a) to the difference in pore pressure in the fault and that outside the fault, p_{out}, presumed to be constant and associated with a very large fluid mass, divided by the square of the characteristic diffusion length, L, $\partial^2 p/\partial x^2 = (p_{\text{out}} - p)/L^2$ such that

$$c_*(p_{\text{out}} - p) = \frac{dp}{dt} + \frac{1}{\phi\left(\beta_f + \beta_\phi\right)}\frac{d\phi}{dt} \tag{11}$$

$c_* = \frac{\kappa}{\phi\left(\beta_f + \beta_\phi\right)\upsilon L^2}$ is the characteristic diffusivity with units 1/s where κ is permeability, and υ is fluid viscosity.

Here c_* is taken to be constant and, as inferred in section 3 above, to be at most $c_* = 1 \times 10^{-6}$/s. We simulate fault slip with (10b) for dilatancy, (11) for pore fluid pressure, (3) for effective stress, (2) and (7) for friction, the loading rate (8), and constant effective normal stress in the absence of dilatancy, using the same Dieterich (1987) approach as in the steady state dilatancy calculations. The results are very similar to the steady state dilatancy calculations (Figure 8). The one difference is a small offset of 0.05 kPa in the inferred value of the rate dependence A_{fit} to lower values relative to $\left(a\sigma_e + \frac{\varepsilon\mu}{\beta}\right)$; the dashed reference line in Figure 8 is $A_{\text{fit}} = 0.7A + 0.05$ kPa.

4. Discussion

For purposes of order of magnitude constraints on frictional properties we take the results from the calculations shown in Figures 7b, 7c, and 8 as indicating that the inferred value of the rate dependence $A_{\text{fit}} \approx \left(a\sigma_e + \frac{\varepsilon\mu}{\beta}\right)$. Comparing this to the fit of the data to equation (9), 330 Pa $\approx \left(a\sigma_e + \frac{\varepsilon\mu}{\beta}\right)$ and, considering the end-member case of $\varepsilon = 0$, requires either that the effective pressure in the source region is low or that the intrinsic instantaneous rate dependence, a, is vanishingly small. Because this rate dependence is expected to increase with temperature theoretically (Nakatani, 2001; Rice et al., 2001) and is observed to do so in limited experiments (Nakatani, 2001), we favor the latter interpretation that the effective pressure is low. Taking $a = 0.006$ as inferred by Chester (1995) for quartz in the brittle rate weakening regime, $\sigma_e = 55$ kPa.

Allowing the fault to dilate, the small value of the sum also requires that the fault zone material is intrinsically weak, as previously inferred by Thomas et al. (2012). Earthquake rates controlled by room temperature dilatancy alone are shown in Figure 5a as the nearly horizontal dashed line. There are actually two dashed lines that overlay one another in the figure that were calculated using the observed tidal shear stress in equation (9) with $A_{\text{fit}} = \varepsilon\mu/\beta = 1.01$ MPa and 0.12 MPa; these values are the earlier inferred $\varepsilon\mu/\beta$ from the San Andreas depth and temperature using room temperature quartz dilatancy data. Allowing contributions from dilatancy and $a\sigma_e$, Figure 9 summarizes the allowable parameters from the fit with (9) where the range of parameters lies between the two solid curves that correspond to values of fault zone compressibility between 1×10^{-3} and 1×10^{-4}/MPa (fault zone porosity of 10 to 1%). To reemphasize the

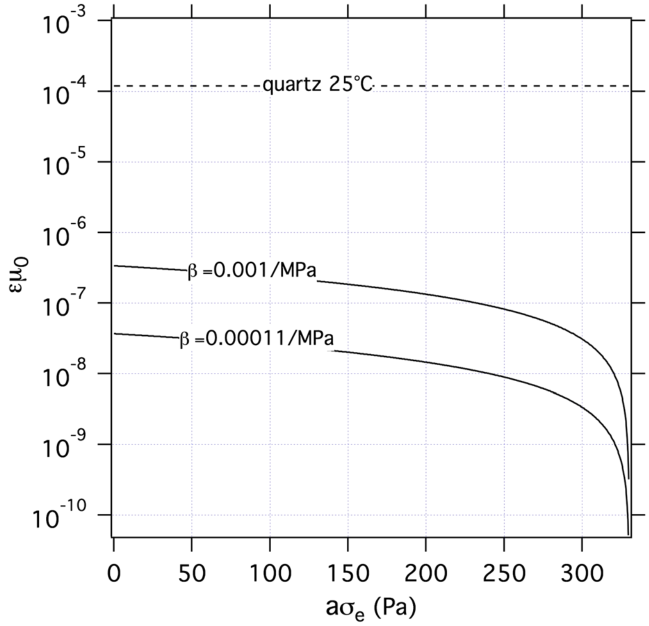

Figure 9. Range of parameters allowed by the fit of the empirical relationship (9) to the continuous family episode onset catalog. Allowable combinations of $\varepsilon\mu$ and $a\sigma_e$ lie between the solid curves that correspond to values of the fault zone compressibility $\beta = 1.03 \times 10^{-3}$ and $\beta = 1.1 \times 10^{-4}$. Shown for reference is the room temperature value of the product $\varepsilon\mu$ for quartz (Table 3).

constraint on $\varepsilon\mu$, the room temperature value for quartz is superimposed as a dashed line and lies well above the upper limit on this product.

A couple of additional constraints on dilatancy are worth noting. The small value of $\varepsilon\mu/\beta$ required by the data is favored by low intrinsic friction coefficients and low dilatancy, independent of the effective normal stress. Experiments on the brittle failure of intact rock show that the pressure dependence of failure strength, the internal coefficient of friction, is a reflection of the dilatancy necessary to produce a throughgoing fault (Brace et al., 1966). Subsequent work on lower strength phyllosilicates (Escartin et al., 1997, 2008) shows that the correlation between dilatancy and pressure dependence extends to these weaker and highly anisotropic materials. Similarly, though it has not been the subject of comprehensive study, for frictional sliding, dilatancy and friction are expected to correlate (Beeler, 2007; Brace, 1978; Escartin et al., 1997, 2008). The dilatancy and friction coefficients of quartz from Marone et al. (1990) when compared with those of muscovite and talc from Scruggs (1997) are consistent with this idea (Table 3). Talc is both the weakest and least dilatant. Accordingly, low frictional strength is expected to correspond to a low dilatancy coefficient and taking talc to be the low strength end-member, with $\varepsilon\mu = 7.28 \times 10^{-6}$, the LFE observations require the deep SAF to be weaker and less dilatant than known measurements made on fault zone materials at room temperature. Regardless of the particular material considered, in light of the expected correlation between intrinsic friction and dilatancy, the SAF LFE data requirement is for a self-consistent, intrinsically weak fault zone material. Also, so long as the pore pressure is elevated well above hydrostatic in the tremor source region, as has been suggested in prior studies (e.g., Becken et al., 2011, and references therein), the pore fluid should be incompressible relative to the porosity and $\beta \approx \phi\beta_\phi$ (Segall & Rice, 1995). The contribution of the compressibility β to the small value of the dilatancy hardening coefficient ($\varepsilon\mu/\beta$) from the data fit in Figure 5 is favored by high and compliant porosity, whereas the temperature and pressure conditions tend to favor small and stiffer porosity. This is an additional contradiction that arises in invoking dilatancy hardening to explain slow slip in the deep crust.

The discrepancy between laboratory measured values of dilatancy (Figure 6), expected compressibility at depth, and the requirements on friction models from the SAF seismicity (Figure 5) can be resolved, at least conceptually, by considering the temperature dependence of friction. Sliding friction and internal friction near the brittle ductile transition are expected to differ from room temperature values, transitioning from stronger pressure dependence (higher friction coefficient) to near zero at the brittle ductile transition (Paterson & Wong, 2006). Since the pressure dependence reflects the relative amount of dilatancy (Escartin et al., 1997, 2008; Beeler, 2007), dilatancy is also expected to effectively vanish at the brittle ductile transition. Even for phyllosilicates, which do not undergo dislocation creep, and lack a clearly defined transition from friction to ductile flow, a reduction in the pressure dependence is expected based on the experiments of Chernak and Hirth (2010). In those tests on antigorite serpentinite between 25 and 620°C, the pressure dependence decreases systematically from near Byerlee's law to <0.3. Thus, in the SAF transition zone where LFEs occur, dilatancy should be systematically reduced for all brittle materials relative to room temperature values. For our triggered frictional slip model, the correlation between LFEs and the tides requires that, in the transition zone, the product of the friction and dilatancy hardening coefficients, $\mu\varepsilon$, is ~5×10^{-7}, whereas the room temperature product for quartz is ~1.2×10^{-4} (Figure 9). Note that in the first section of this paper we had dismissed extreme intrinsic weakness as an explanation for the lack of dependence of earthquake rates on the

Table 3
Room Temperature Friction and Dilatancy Coefficients

Material	μ	ε
**Talc	0.14	5.2×10^{-5}
**Muscovite	0. 37	1.5×10^{-4}
*Quartz	0.7	1.7×10^{-4}

*Values from Segall and Rice (1995) based on the experiments of Marone et al. (1990). **Scruggs (1997).

normal stress tides based on a lack of experimental verification. That the assumption of undrained frictional deformation also requires intrinsic weakness leaves no alternative.

The inference from friction models in this study, that pore fluid pressure is lithostatic on the deep extent of the SAF, is consistent with previous geophysical studies (e.g., Becken et al., 2011, and references therein). Because these LFEs occur at depths between 15 and 30 km, and at temperatures between 350 and 600°C, below the conventional brittle-ductile transition, porosity is not expected to be maintained long-term due to crystal plasticity. As minerals deform at elevated temperature, pore space collapses reducing permeability, leading to an increase in pore pressure. The implied weakness is reminiscent of inferences of the strength of subduction zones based on the fault orientation and a force balance (Wang & He, 1999), and from measurements of subduction zone heat flow (Gao & Wang, 2014).

The requirement that the deep SAF is undrained at the period of the semidiurnal tides, t_p, places constraints on the shear zone thickness and the fluid diffusivity, α. We distinguish between the diffusivity c_*, having units of 1/s that is generally constrained by our analysis, and the fluid diffusivity that has units of m^2/s and determines the length scale of the fluid diffusion. For example, if the diffusion distance is taken as the half-width of the shear zone, $L/2$, then $L = 2\sqrt{\alpha t_p}$, and if the shear zone width corresponds to the expectation from field studies (Chester & Chester, 2000; Chester et al., 2004) and is of the order of 0.1 to 1 mm, then the upper bound on the diffusion coefficient is 5.6×10^{-12} m^2/s. That is, the fault may be undrained on time periods longer than the semidiurnal (t_p = 44,712 s), making our estimate possibly higher than the actual value.

When the constraints from the triggered frictional slip model are compared with those from previously published friction modulation models (Ader et al., 2012; Beeler et al., 2013), significant similarities are found. First, at constant normal stress, all of these models predict an in-phase relationship between the earthquake rates for the semidiurnal shear tides and reasonable values of the slip-weakening distance. Furthermore, the fundamental constraint from all models is on the same rheological parameter, the instantaneous rate dependence of frictional strength. Finally, to a first approximation, the constraints from all models are the same. While it is unfortunate these models cannot be easily distinguished from one another on the basis of the strength of the tidal correlation itself, on the other hand, it is notable that these and other seismicity rate models for friction (Dieterich, 1994) are controlled by the same rheological property. An instantaneous rate dependence is ubiquitous in low- and high-temperature rock deformation: friction (Dieterich, 1979), fracture (Scholz, 1968), crack growth (Atkinson & Meredith, 1987a, 1987b), pressure solution (Niemeijer et al., 2002), and plasticity (Mares & Kronenberg, 1993); therefore, there is a general empirical expectation that all brittle and transition zone deformation will exhibit this kind of behavior (Beeler et al., 2007, and references therein). It is encouraging that the nonlinear form of the rate dependence is found in experiments, expected on a theoretical basis (Nakatani, 2001; Rice et al., 2001), largely independent of the particular low-temperature deformation mechanism (e.g., crack growth and plasticity) and is consistent with deep non-linear tidal correlations in a number of environments (Houston, 2015; Ide & Tanaka, 2014; Royer et al., 2015; Thomas et al., 2009, 2012; Yabe et al., 2015). That said, the constraints on dilatancy, friction, and diffusion developed in this study for a triggering model have not been considered for modulation. While there is no expectation that significantly different constraints will arise for modulated slip, nonetheless, this remains a topic for further investigation.

The particular form of rate-dependent dilatancy hardening (Segall & Rice, 1995) used in our study has been invoked as a control on the slip speed during slow-slip events in simulations (Liu & Rubin, 2010; Segall et al., 2010). Since our result suggests that this dilatancy does not play a role in the onset of slip events on the San Andreas, it also raises the question whether there are similar limitations on the role of dilatancy on modulating slip rate during slow events. Regardless, given the limitations of the slider-block model used (see immediately below), some care should be exercised in applying our conclusions generally to other locales. The results are limited to the deep SAF and whether that result applies elsewhere will depend on the tidal amplitude (which is higher for shear stress in Cascadia, for example), the particular stress components that are associated with the correlation, and strength of the tidal correlations. The analysis would have to be repeated in any region in which the slow slip is well-resolved.

To that end, measurements of the instantaneous dependence of fault strength on slip rate, such as a in equation (2), and the hydraulic properties of shear zones could be routinely made in laboratory experiments at the elevated temperatures and pressures found in the source region of the SAF LFEs and elsewhere at deep crustal conditions (e.g., Boettcher et al., 2007). Shear dilatancy as measured by ε in equation (4) and the detailed slip and rate dependencies of dilatancy (Figure 6) may also be accessible at these conditions by monitoring pore volume. It is likely that the fundamental nature of dilatancy at high temperature and pressure differs from that at room temperature and might most easily be determined experimentally using a nonreactive phase such as argon as the pore fluid. Furthermore, lab slip rates overlap the range of natural plate motion rates and fault slip rates during episodic slow slip events; thus, experiments can be conducted at the actual pressure, temperature, and slip rate conditions and, except the difference in scale (fault length and shear zone thickness), results can be applied to the Earth without extrapolation. Such experiments are needed at conditions appropriate for the deep San Andreas in central California and for the transition zone in Cascadia and other subduction environments. These are among the highest research priorities for laboratory studies of deep crustal fault mechanics.

As discussed briefly in the introduction there are a large number of proposed models of ETS phenomenon, but only a limited number that have been used to directly address the correlation between the tides and low-frequency earthquakes or tremor. The rheological models underlying our implementation are applied using a single degree of freedom, spatially dimensionless slider block model where large-scale aseismic slip and small-scale seismic slip are used interchangeably, assuming a proportionality between slip rate and seismicity rate, and where the seismic sources do not recur. In contrast within the rheologically heterogeneous natural source region, the interactions between small-scale seismicity and large-scale aseismic slip are complex, leading to back and forward propagating slip events (Bletery et al., 2017; Houston et al., 2011; Rubin, 2011), varying propagation speeds (Rubin, 2011), and seismicity that consists of repeating sources (Shelly et al., 2007). Progress in understanding correlations among the tides, seismicity, and slip events and the mechanics of deep slip requires dimensioned heterogeneous rheological models such as Skarbek et al. (2012, 2014) and Dublanchet et al. (2013). Application of these models to tidal triggering and slip modulation may provide guidance in understanding circumstances where the seismicity rate and fault slip rate are proportional, the relative proportions of triggered and modulated seismicity in the deep crust, and the dependence of observable quantities on the density and magnitude of the heterogeneity.

5. Limitations

There are assumptions related to scale and the properties of the source in the triggering model that are not well-justified. Though the calculations are not strongly dependent on stiffness, the particular choice for the slipping portion of the fault surrounding an LFE source (6×10^{-7} MPa/μm) is ad hoc. An especially unrealistic aspect of the triggering calculations is the assumption of a population of events, whereas it would be more consistent with the observations of episodic clustering of LFEs (Figure 3) to represent the triggered source as a single repeating event. While this choice is hard to justify on conceptual grounds, there are artifacts that arise in calculations of a repeating source using rate and state friction and tidal loading that have little or no observational basis. Essentially, the problems are phase-locking of occurrence with the imposed stress, and resonances. When simulating triggered slip with perfectly periodic stressing, these artifacts arise because at constant loading rate, rate and state friction produces perfectly periodic recurrence. There are no clear natural counterparts to this kind of behavior, and the primary example in which a repeating rate and state source with resonance has been used to model tidal correlations (Ader et al., 2014) is the application to background seismicity rates in Nepal. That study shows enhanced tidal correlations about a characteristic period that are much stronger than those in our calculations. Additionally, in that study, the repeating source has a finite dimension so it is not completely clear whether the enhancement is due to the dimension, the periodicity of the source, or both. While avoiding enhancement artifacts of the friction equations was central to our choice to adopt the population approach of Dieterich (1987), developing dimensioned repeating source models for triggered LFE sequences on the SAF and elsewhere is an important future consideration.

There are wide variations in the degree that individual LFE family occurrences are episodic (Shelly & Johnson, 2011) and in their tidal sensitivity (Thomas et al., 2012), and our study considers the average behavior of LFEs and NVT. In particular there are spatial variations in tidal shear stress sensitivity and some LFE families that show systematic correlation with both positive and negative normal stress that are obscured by analyzing the entire catalog. There are similar correlations of LFE families with compressive normal tidal stress in Cascadia (Royer et al., 2015, their Figure 4 and discussion section 5.1). Highly variable normal stress correlations likely indicate nonuniform effective normal stress and poroelastic and hydraulic properties. For example, correlations with compressive normal stress can result from partially drained conditions introducing a phase lag between normal stress and pore pressure. Modeling families individually is an important next step in determining spatial variation of the fault properties on the deep SAF.

While future experiments at hypocentral conditions should provide friction and dilatancy data that can be applied directly in models of slow slip and nonvolcanic tremor, a significant remaining experimental challenge is understanding the physics of rate-dependent dilatancy in the first place, including the behaviors that are known and not included in existing models. For example, quartzofeldspathic materials (Marone et al., 1990; Marone & Kilgore, 1993) and phyllosilicate gouges (Scruggs, 1997) undergo changes in the displacement rate of dilatancy when slip rate is changed that are not included in the Segall and Rice (1995) equations. The implications of such effects for dilatancy hardening and triggered seismicity are unknown. Regardless of the particular form of dilatancy, whether it be as parameterized by Segall and Rice (1995) or a more complicated response, the experimental rock mechanics understanding of dilatancy strains, based on the early rock failure tests of Brace et al. (1966), is that these are pressure independent. Accordingly, dilatancy represents the work done against the normal stress necessary to allow shear deformation, and while the work is an increasing function of normal stress, the normal strain is not. These ideas are consistent with the Segall and Rice (1995) treatment. In the deep crust where ductile processes tend to reduce porosity, raise the pore pressure, and lead to undrained deformation, the mechanical contributions from slip dilatancy will increase in importance and oppose the intrinsic rate dependence that is reduced under the same conditions. If this conceptual model holds, where there is correlation of deep seismicity with the tides (Houston, 2015; Royer et al., 2015), and where high pore pressure is invoked, dilatancy likely places significant limits on the possible rate of fault slip (Segall & Rice, 1995).

6. Conclusions

The SAF LFE family occurrences are clustered, correlated with the tides, and the majority of families have cluster durations much shorter than the daily tidal period. If those durations are interpreted as that of slip episodes, the very short duration precludes slip modulation on the time scale of episodes from explaining correlation between earthquake rates and the tides. The clusters are apparently triggered by the tides, and we determine constraints on the deep fault rheology by assuming that episode onsets represent the onset of truly triggered fault creep of the fault surrounding the LFE source. By assuming that that frictional slip is dilatant (Segall & Rice, 1995) and that the fault zone is undrained, the strong correlation between the Earth tides and LFE rates constrains the diffusivity and product of the friction and dilatancy coefficients. Undrained triggered frictional slip predicts no sensitivity to the tidal normal stress (Hawthorne & Rubin, 2010), and a seismicity rate in phase with the tidal shear stress. In this context the observations require that the diffusivity in the source region is less than 1×10^{-6}/s and that the product of the friction and dilatancy coefficients to be at most 5×10^{-7}. This product is orders of magnitude smaller than observed at room temperature for quartz, also smaller than for weaker and less dilatant materials at 25°C. In the context of this friction model the observations require low intrinsic friction, low dilatancy, and lithostatic pore fluid pressures.

Appendix A: Tidal Triggering With Poroelasticity

A one-dimensional fluid mass balance requires

$$\frac{dm}{dt} = \frac{\rho\kappa}{v}\frac{\partial^2 p}{\partial x^2} \tag{A1}$$

(Segall & Rice, 1995), where m is fluid mass per unit volume, ρ is fluid density, κ is permeability, and υ is fluid viscosity. For this implementation x is the fault normal direction. Considering that fluid mass per unit volume $m = \rho\phi$, where ϕ is porosity, leads to

$$\frac{dm}{dt} = \rho\frac{d\phi}{dt} + \phi\rho\beta_f\frac{dp}{dt} \tag{A2}$$

(Segall & Rice, 1995), where the fluid compressibility is $\beta_f = 1/\rho d\rho/dp$. Faults and joints are preferentially compliant normal to the discontinuity (Brown & Scholz, 1986; Cocco & Rice, 2002), and for simplicity, we consider this compliance to dominate the elastic deformation of the fault zone in response to arbitrary changes in the stress state such as from the tides. Theoretical considerations and preliminary measurements on simulated fault gouges are consistent with this idea (Beeler & Lockner, 2004; Cocco & Rice, 2002). Thus, in (A2), we characterize the change in porosity $d\phi/dt$ as depending entirely on applied normal stress and pore pressure, or

$$\frac{d\phi}{dt} = \phi\beta_\phi \frac{dp}{dt} + \phi\beta_\phi{}' \frac{d\sigma_n}{dt}, \tag{A3}$$

where the pore compressibilities due to changes in pore pressure and normal stress are $\beta_\phi = 1/\phi d\phi/dp$ and $\beta_\phi{}' = 1/\phi d\phi/d\sigma_n$, respectively. Combining (A2) and (A3), results in

$$\frac{dm}{dt} = \rho\left(\beta\frac{dp}{dt} + \phi\beta_\phi{}'\frac{d\sigma_n}{dt}\right), \tag{A4a}$$

where, following Segall and Rice (1995), the combined compressibility of the pore space and fluid in response to changes in pore pressure is $\beta = \phi(\beta_\phi + \beta_f)$. Under undrained conditions the fluid mass in the fault zone does not change and (A4a) defines a Skempton-like coefficient for pore pressure (e.g., Beeler & Lockner, 2002, 2004), that is,

$$\frac{dp}{d\sigma_n} = B' = \frac{\beta_\phi{}'}{\beta_f + \beta_\phi}. \tag{A4b}$$

Since the pore compressibility in response to normal stress is bounded to be $\beta_\phi{}' \le \beta_\phi$, then $0 \le B' \le 1$.

More general time-dependent changes in pore pressure due to the tides can be represented by combining (A4a) and (A1).

$$\frac{\kappa}{\beta v}\frac{\partial^2 p}{\partial x^2} = \frac{dp}{dt} + B'\frac{d\sigma_n}{dt}. \tag{A5a}$$

Again following Segall and Rice (1995), for 1-D diffusion normal to the fault, we equate the second spatial derivative of pore pressure to the difference in pore pressure in the fault and that outside the fault, p_{out}, presumed to be constant and associated with a very large fluid mass, divided by the square of the characteristic diffusion length, L, $\partial^2 p/\partial x^2 = (p_{\text{out}} - p)/L^2$ such that

$$C_*(p_{\text{out}} - p) = \frac{dp}{dt} + B'\frac{d\sigma_n}{dt}. \tag{A5b}$$

and $C_* = \frac{\kappa}{\beta v L^2}$ is the characteristic diffusivity with unit 1/time.

To represent triggered frictional slip we used the standard form of rate and state friction (Dieterich, 1979; Ruina, 1983), equation (2) in the main text of this paper,

$$\tau = \sigma_e\left(\mu_0 + a\ln\frac{V}{V_0} + b\ln\frac{\theta V_0}{d_c}\right), \tag{A6a}$$

where θ is the state variable of Ruina (1983) with steady state value $\theta_{ss} = V_0/V$, a and b are coefficients that are small relative to μ_0, $b > a$ (rate weakening), and σ_e is the effective normal stress, $\sigma_n - p$. In these calculations the state variable is

$$\frac{d\theta}{dt} = -\frac{V\theta}{d_c}\ln\left(\frac{V\theta}{d_c}\right) \tag{A6b}$$

(Ruina, 1983). The results are thought to be independent of the choice of state variable (Beeler & Lockner, 2003), but that has not been tested in these calculations. The state variable represents strength losses associated with increasing slip rate. Loading consists of a nominal constant rate of stressing that represents tectonic loading and an oscillating stress representing the tides that is imposed as a body force,

$$\frac{d\tau}{dt} = k(V_L - V) + \frac{2\pi\Delta\tau}{t_p}\cos\left(\frac{2\pi t}{t_p}\right), \tag{A7a}$$

where we have represented the tidal shear stress as a simple sine function. k is the stiffness, $\Delta\tau$ is the amplitude of the tidal shear stress, t_p is the tidal period, and V_L is the loading velocity. On the San Andreas the shear and normal tides are out of phase with each other, defining their individual influence on the low-frequency

Table A1
Parameters for Triggered Frictional Slip With Poroelasticity

Parameter	Value
μ_0	0.70
a	0.007
b	0.012
d_c	3 μm
V_0	1 μm/s
V_L	0.001 μm/s
k	6×10^{-7} MPa/μm
$\Delta\tau$	2.3×10^{-4} MPa
$\Delta\sigma_n$	2.3×10^{-3} MPa
t_p	44,712 s
B'	1.0
p_{out}	489.95 MPa
σ_n^0	490 MPa
θ_0	10,000 s
N	500

earthquake rates (Thomas et al., 2009; 2012). In contrast, in these calculations for simplicity, the tidal normal stress with amplitude $\Delta\sigma_n$ is exactly in phase with the variations in shear stress,

$$\frac{d\sigma_n}{dt} = \frac{2\pi\Delta\sigma_n}{t_p}\cos\left(\frac{2\pi t}{t_p}\right). \tag{A7b}$$

The calculations follow the approach of Dieterich (1987) in spirit and consist of a population of N sources that are initially far from failure with identical frictional properties. The initial phase of the tidal stress for these sources is distributed uniformly over the tidal period t_p. When $\Delta\tau = 0$ and $\Delta\sigma_n = 0$, the failure rate of the population, the seismicity rate, is constant at N/t_p. The friction parameters, fault properties, stresses, tides, and pore pressure (Table A1) were selected to match known conditions on the deep San Andreas and to produce earthquake rates that are qualitatively consistent with the observations. These triggering calculations were conducted over a range of values of the diffusivity c_* from undrained, 1×10^{-10}/s, to drained, 3×10^{-2}/s, relative to the semidiurnal tides, to examine the phase of peak earthquake rate relative to peak stress of the imposed tides (Figure A1, solid symbols). The fault zone pore pressure is decoupled from shear stress and slip rate. In the calculations the shear tide is 10 times smaller than normal stress tide.

The phase of the peak earthquake rate and the phase of the effective stress in these calculations depend on c_*, the phase difference between the shear and normal tides, the Skempton-like coefficient B', the nominal friction coefficient, and the relative sizes of the shear and normal stress tides. To understand the range of possible phases of these peaks we first consider the phase of peak earthquake rate for the end-member case of undrained pore fluid pressure. For undrained conditions, c_* in (A5b) is negligible and pore pressure oscillates in phase with the normal stress. Because $B' = 1$ in these calculations, the difference between normal stress and pore pressure, the effective stress, does not vary at undrained conditions so there is no contribution from the normal stress tides to the earthquake rate (Hawthorne & Rubin, 2010). The earthquake rate follows, essentially in phase the shear stress tides, just as it does in models without pore pressure (e.g., Dieterich, 1987). For a sine the peak of the shear tide is at $\pi/2$, so that is the phase of the undrained peak earthquake rate (Figure A1).

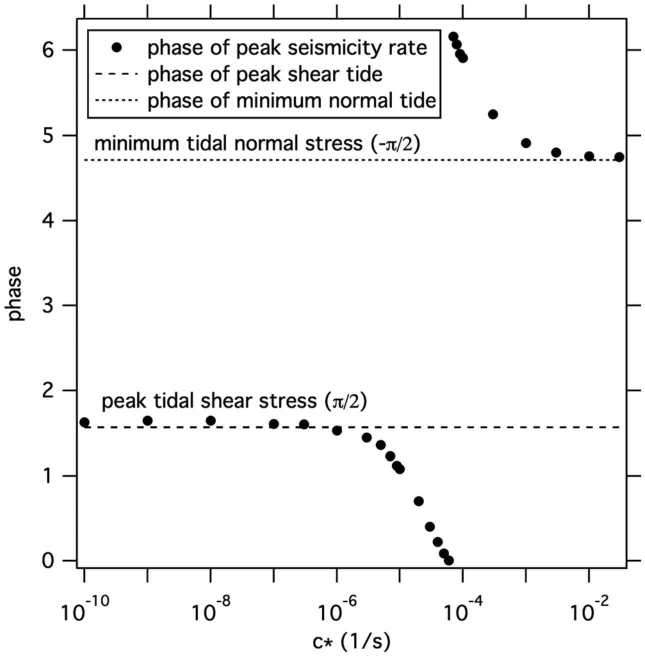

Figure A1. Phase of peak seismicity rate as a function of diffusivity for triggered slip with poroelasticity (no dilatancy). The shear and normal tides are in phase, and the amplitude of the normal tide is 10 times the shear tide (2.3 and 0.23 kPa, respectively). The parameters used in the simulations are listed in Table A1. The dashed reference line is the phase of the peak shear stress tide ($\pi/2$); the dotted reference line is the phase of the minimum normal stress tide ($-\pi/2$), the maximum in unloading normal stress.

For drained conditions c_* is large, there is no oscillation of pore pressure with normal stress and the effective stress is the applied normal stress minus p_{out}. The earthquake rate then is sensitive to both shear and normal tides. Since there is no phase shift between the shear and normal tides in our calculations, the maximum influence of the normal tide is the minimum of the sine function, at phase $-\pi/2$. At drained conditions the maximum earthquake rate is dominated by the normal stress tides when $\mu\Delta\sigma >> \Delta\tau$, as is the case in our calculations where friction coefficient is high ($\mu = 0.7$), and the normal stress tide is 10 times larger than for shear stress. Accordingly, the drained peak earthquake rate is at $-\pi/2$.

At intermediate values of c_*, the phase of the peak earthquake rate is between these two end-member cases, as is shown in the summary plot (Figure A1). As c_* is increased from the lowest value (undrained), corresponding to shortening of the diffusion time, the fault moves to become progressively more drained and the peak rate becomes out of phase with the shear tides. As c_* is progressively increased from undrained conditions, the shift involves two effects: (1) the increased influence of normal stress, described above, and (2) a phase shift between the peak normal stress and peak pore pressure. For this fault model, pore pressure in the fault zone is entirely decoupled from shear stress and from slip rate; thus, the contribution can be determined from equations (A5b) and (A7b). The peak in pore pressure shifts to lower phase as the fault becomes more drained. The net influence of increasing effective normal stress and a phase shift in peak pore pressure is the phase shift in earthquake rate shown in Figure A1.

Here the direction of the phase shift in the earthquake rate with changing c_* is not important for our purposes, though phase shifts in natural data may be diagnostic of the underlying processes (e.g., Thomas et al., 2009; 2012). As the observations (Figure 5a) are an in-phase relationship between shear stress tide and the maximum earthquake rate, consistent with the undrained end-member, these calculations suggest that the diffusivity on the deep San Andreas is less than approximately 1×10^{-6}/s.

Acknowledgments
The central San Andreas LFE catalog (Shelly & Hardebeck, 2010; Shelly, 2017) was used in this paper. That data and the technical aspects of catalog generation are available in those publications and their supplements. All of the source data used in the figures and analysis are from the published catalog. There is no new original source data in this report. Discussions of tidal triggering and modulation with Allan Rubin, David Locker, Heidi Houston, and Evelyn Roeloffs are greatly appreciated. This contribution was significantly improved in response to USGS internal reviews by Nicholas Van der Elst and Carolyn Morrow and JGR-SE reviews by Paul Segall, Jessica Hawthorne, Pablo Ampuero, and the editor Yehuda Ben-Zion. The idea of "apparent" triggering arose in response to Pablo's suggestions.

References

Ader, T. J., Ampuero, J.-P., & Avouac, J.-P. (2012). The role of velocity-neutral creep on the modulation of tectonic tremor activity by periodic loading. *Geophysical Research Letters*, *39*, L16310. https://doi.org/10.1029/2012GL052326

Ader, T. J., Lapusta, N., Avouac, J.-P., & Ampuero, J.-P. (2014). Response of rate- and -state seismogenic faults to harmonic shear-stress perturbations. *Geophysical Journal International*, *198*, 385–413.

Atkinson, B. K., & Meredith, P. G. (1987a). The theory of subcritical crack growth with applications to minerals and rocks. In B. K. Atkinson (Ed.), *Fracture Mechanics of Rock* (pp. 111–166). New York: Elsevier.

Atkinson, B. K., & Meredith, P. G. (1987b). Experimental fracture mechanics data for rocks and minerals. In B. K. Atkinson (Ed.), *Fracture mechanics of rock* (pp. 477–525). New York: Elsevier.

Becken, M., Ritter, O., Bedrosian, P. A., & Weckmann, U. (2011). Correlation between deep fluids, tremors and creep along the central San Andreas Fault. *Nature*, *480*, 87–90.

Beeler, N. M. (2007). Laboratory-observed faulting in intrinsically and apparently weak materials: Strength, seismic coupling, dilatancy, and pore fluid pressure. In T. Dixon & C. Moore (Eds.), *The seismogenic zone of subduction thrust faults* (chapter 13, pp. 370–449). New York: Columbia University Press.

Beeler, N. M., & Lockner, D. A. (2002). Stress-induced anisotropic poroelasticity in granular materials and porous rock. *Eos, Transactions American Geophysical Union*, *83*, F1375.

Beeler, N. M., & Lockner, D. A. (2003). Why earthquakes correlate weakly with Earth tides: The effects of periodic stress on the rate and probability of earthquake occurrence. *Journal of Geophysical Research*, *108*, 2391. https://doi.org/10.1029/2001JB001518

Beeler, N. M., & Lockner, D. A. (2004). The anisotropic poroelastic response of a granular fault gouge. *Eos, Transactions American Geophysical Union, 85*(17), Jt. Assem. Suppl., Abstract T31A-07.

Beeler, N. M., Thomas, A. M., Burgmann, R., & Shelly, D. R. (2013). Inferring fault rheology from low frequency earthquakes on the San Andreas Fault. *Journal of Geophysical Research*, *118*, 5976–5990. https://doi.org/10.1002/2013JB010118

Beeler, N. M., & Tullis, T. E. (1997). The roles of time and displacement in velocity dependent volumetric strain of fault zones. *Journal of Geophysical Research*, *102*, 22,595–22,609.

Beeler, N. M., Tullis, T. E., Kronenberg, A. K., & Reinen, L. A. (2007). The instantaneous rate dependence in low temperature laboratory rock friction and rock deformation experiments. *Journal of Geophysical Research*, *112*, B07310. https://doi.org/10.1029/2005JB003772

Ben-Zion, Y. (2012). Episodic tremor and slip on a frictional interface with critical zero weakening in elastic solid. *Geophysical Journal International*, *189*, 1159–1168. https://doi.org/10.1111/j.1365-246X.2012.05422.x

Bletery, Q., Thomas, A. M., Hawthorne, J. C., Skarbek, R. M., Rempel, A. W., & Krogstad, R. D. (2017). Characteristics of secondary slip fronts associated with slow earthquakes in Cascadia. *Earth and Planetary Science Letters*. https://doi.org/10.1016/j.epsl.2017.01.046

Boettcher, M. S., Hirth, J. G., & Evans, B. (2007). Olivine friction at the base of oceanic seismogenic zone. *Journal of Geophysical Research*, *112*, B0125. https://doi.org/10.1029/2006JB004301

Brace, W. F. (1978). Volume changes during fracture and frictional sliding. *Pure and Applied Geophysics*, *116*, 603–614.

Brace, W. F., Paulding, B. W., & Scholz, C. H. (1966). Dilatancy in the fracture of crystalline rock. *Journal of Geophysical Research*, *71*, 3939–3953. https://doi.org/10.1029/JZ071i016p03939

Brown, S. R., & Scholz, C. H. (1986). Closure of rock joints. *Geophysical Research Letters*, *91*, 4939–4948.

Bufe, C. G., Harsh, P. W., & Burford, R. O. (1977). Steady-state seismic slip—A precise recurrence model. *Geophysical Research Letters*, *4*, 91–94.

Burnham, C. W., Holloway, J. R., & Davis, N. F. (1969). Thermodynamic properties of water to 1,000°C and 10,000 bars. *Geological Society of America Special Papers*, *132*, 96.

Chernak, L. J., & Hirth, G. (2010). Deformation of antigorite serpentinite at high temperature and pressure. *Earth and Plantary Science Letters*, *296*, 23–33.

Chester, F. M. (1995). A rheologic model for wet crust applied to strike-slip faults. *Journal of Geophysical Research*, *100*, 13,033–13,043.

Chester, F. M., & Chester, J. S. (2000). Stress and deformation along wavy frictional faults. *Journal of Geophysical Research*, *105*(B10), 23,421–23,430. https://doi.org/10.1029/2000JB900241

Chester, F. M., Chester, J. S., Kirschner, D. L., Schultz, S. E., & Evans, J. P. (2004). Structure of large-displacement, strike-slip fault zones in the brittle continental crust. In G. D. Karner (Eds.), *Rheology and deformation in the lithosphere at continental margins*. New York: Columbia University Press.

Cocco, M., & Rice, J. R. (2002). Pore pressure and poroelasticity effects in Coulomb, stress analysis of earthquake interactions. *Journal of Geophysical Research*, *107*(B2), ESE 2–1–ESE 2–17, ⊠. https://doi.org/10.1029/2000JB000138

Dieterich, J. H. (1979). Modeling of rock friction 1. Experimental results and constitutive equations. *Journal of Geophysical Research*, *84*, 2161–2168.

Dieterich, J. H. (1987). Nucleation and triggering of earthquake slip: Effect of periodic stresses. *Tectonophysics*, *144*, 127–139.

Dieterich, J. H. (1994). A constitutive law for rate of earthquake production and its application to earthquake clustering. *Journal of Geophysical Research*, *99*, 2601–2618.

Dragert, H., Wang, K., & James, T. S. (2001). A silent slip event on the deeper Cascadia subduction interface. *Science*, *292*, 1525–1528.

Dublanchet, P., Bernard, P., & Favreau, P. (2013). Interactions and triggering in a 3-D rate-and-state asperity model. *Journal of Geophysical Research: Solid Earth*, *118*, 2225–2245. https://doi.org/10.1002/jgrb.50187

Escartin, J., Andreani, M., Hirth, G., & Evans, B. (2008). Relationships between the microstructural evolution and the rheology of talc at elevated pressures and temperatures. *Earth and Planetary Science Letters*, *268*, 463–475.

Escartin, J., Hirth, G., & Evans, B. (1997). Nondilatant brittle deformation of serpentinites; implications for Mohr-Coulomb theory and the strength of faults. *Journal of Geophysical Research*, *102*, 2897–2913.

Gao, X., & Wang, K. (2014). Strength of stick-slip and creeping subduction megathrusts from heat flow observations. *Science*, *345*, 1038–1041.

Hawthorne, J. C., & Rubin, A. M. (2010). Tidal modulation of slow slip in Cascadia. *Journal of Geophysical Research*, *115*, B09406. https://doi.org/10.1029/2010JB007502

Hawthorne, J. C., & Rubin, A. M. (2013). Tidal modulation and back-propagating fronts in slow slip events simulated with a velocity-weakening to velocity-strengthening friction law. *Journal of Geophysical Research*, *118*, 1216–1239. https://doi.org/10.1002/jgrb.50107

Hayman, N. W., & Lavier, L. L. (2013). The geologic record of deep episodic tremor and slip. *Geology*, *42*, 195–198.

Houston, H. (2015). Low friction and fault weakening revealed by rising sensitivity of tremor to tidal stress. *Nature Geoscience*, *8*(5), 409–415. https://doi.org/10.1038/ngeo2419

Houston, H., Delbridge, B. G., Wech, A., & Creger, K. C. (2011). Rapid tremor reversals in Cascadia generated by a weakened plate interface. *Nature Geoscience*, *4*, 404–409. https://doi.org/10.1038/ngeo1157

Ide, S., Shelly, D. R., & Beroza, G. C. (2007). Mechanism of deep low frequency earthquake: Further evidence that deep nonvolcanic tremor is generated by shear slip on the plate interface. *Geophysical Research Letters*, *34*, L03308. https://doi.org/10.1029/2006GL028890

Ide, S., & Tanaka, Y. (2014). Controls on plate motion by oscillating tidal stress: Evidence from deep tremors in western Japan. *Geophysical Research Letters*, *41*, 3842–3850. https://doi.org/10.1002/2014GL060035

Kao, H., Wang, K., Dragert, H., Kao, J. Y., & Rogers, G. (2010). Estimating seismic moment magnitude (*Mw*) of tremor bursts in northern Cascadia: Implications for the "seismic efficiency" of episodic tremor and slip. *Geophysical Research Letters*, *371*, L19306. https://doi.org/10.1029/2010GL044927

Lachenbruch, A. H., & Sass, J. H. (1973). Thermo-mechanical aspects of the San Andreas Fault System. In *Proceedings of the Conference on the Tectonic Problems of the San Andreas Fault System* (pp. 192–205). Stanford, CA: Stanford University Press.

Lambert, A., Kao, H., Rogers, G., & Courtier, N. (2009). Correlation of tremor activity with tidal stress in the northern Cascadia subduction zone. *Journal of Geophysical Research*, *114*, B00A08. https://doi.org/10.1029/2008JB006038

Liu, Y., & Rice, J. R. (2007). Spontaneous and triggered aseismic deformation transients in a subduction fault model. *Journal of Geophysical Research*, *112*, B09404. https://doi.org/10.1029/2007JB004930

Liu, Y., & Rubin, A. M. (2010). Role of fault gouge dilatancy on aseismic deformation transients. *Journal of Geophysical Research*, *115*, B10414. https://doi.org/10.1029/2010JB007522

Lockner, D. A., & Beeler, N. M. (1999). Premonitory slip and tidal triggering of earthquakes. *Journal of Geophysical Research*, *104*, 20,133–20,151.

Mares, V. M., & Kronenberg, A. K. (1993). Experimental deformation of muscovite. *Journal of Structural Geology*, *15*, 1061–1075.

Marone, C., & Kilgore, B. (1993). Scaling of the critical slip distance for seismic faulting with shear strain in fault zones. *Nature*, *362*, 618–621.

Marone, C., Raleigh, C. B., & Scholz, C. H. (1990). Frictional behavior and constitutive modeling of simulated fault gouge. *Journal of Geophysical Research*, *95*, 7007–7025.

Métivier, L., de Viron, O., Conrad, C., Renaul, S., Diament, M., & Patau, G. (2009). Evidence of earthquake triggering by the solid Earth tides. *Earth and Planetary Science Letters*, *278*, 370–375.

Moore, D. E., & Lockner, D. A. (2007). Friction of the smectite clay montmorillonite: A review and interpretation of data. In T. Dixon & C. Moore (Eds.), *The seismogenic zone of subduction thrust faults* (chapter 13, pp. 317–345). New York: Columbia University Press.

Morrow, C., & Byerlee, J. (1989). Experimental studies of compaction and dilatancy during frictional sliding on faults containing gouge. *Journal of Structural Geology*, *11*, 815–825.

Nadeau, R. M., & Johnson, L. R. (1998). Seismological studies at Parkfield VI: Moment release rates and estimates of source parameters for small repeating earthquakes. *Bulletin of the Seismological Society America*, *88*, 790–814.

Nakatani, M. (2001). Conceptual and physical clarification of rate and state friction: Frictional sliding as a thermally activated rheology. *Journal of Geophysical Research*, *106*, 13,347–13,380.

Niemeijer, A. R., Spiers, C. J., & Bos, B. (2002). Compaction creep of quartz sand at 400–600°C: experimental evidence for dissolution-controlled pressure solution. *Earth and Planetary Science Letters*, *195*, 261–275.

Obara, K. (2002). Nonvolcanic deep tremor associated with subduction in southwest Japan. *Science*, *296*, 1679–1681. https://doi.org/10.1126/science.1070378

Paterson, M. S., & Wong, T.-F. (2006). *Experimental rock deformation: The brittle field* (Vol. 347). New York: Springer-Verlag.

Perfettini, H., & Avouac, J. (2004). Postseismic relaxation driven by brittle creep: A possible mechanism to reconcile geodetic measurements and the decay rate of aftershocks, application to the Chi-Chi earthquake, Taiwan. *Journal of Geophysical Research*, *109*, B02304. https://doi.org/10.1029/2003JB002488

Perfettini, H., & Schmittbuhl, J. (2001). Periodic loading on a creeping fault: Implications for tides. *Geophysical Research Letters*, *28*, 435–438.

Rice, J. R., Lapusta, N., & Ranjith, K. (2001). Rate and state dependent friction and the stability of sliding between elastically deformable solids. *Journal of the Mechanics and Physics Solids*, *49*, 1865–1898.

Royer, A. A., Thomas, A. M., & Bostock, M. G. (2015). Tidal modulation and triggering of low-frequency earthquakes in northern Cascadia. *Journal of Geophysical Research: Solid Earth*, *120*, 384–405. https://doi.org/10.1002/2014JB011430

Rubin, A. M. (2011). Designer friction laws for bimodal slow slip propagation speeds. *Geochemistry, Geophysics, Geosystems*, *12*, Q04007. https://doi.org/10.1029/2010GC003386

Ruina, A. L. (1983). Slip instability and state variable friction laws. *Journal of Geophysical Research*, *88*, 10,359–10,370.

Savage, H. M., & Marone, C. (2007). Effects of shear velocity oscillations on stick-slip behavior in laboratory experiments. *Journal of Geophysical Research*, *112*, B02301. https://doi.org/10.1029/2005JB004238

Scholz, C. H. (1968). Mechanism of creep in brittle rock. *Journal of Geophysical Research*, *73*, 3295–3302.

Scruggs, V. J. (1997). Frictional constitutive properties and related microstructures of albite, muscovite, biotite and talc, PhD dissertation, Brown University, Providence, Rhode Island.

Segall, P., & Bradley, A. M. (2012). Slow-slip evolves into megathrust earthquakes in 2D numerical simulations. *Geophysical Research Letters*, *39*, L18308. https://doi.org/10.1029/2012GL052811

Segall, P., & Rice, J. R. (1995). Dilatancy, compaction, and slip instability of a fluid infiltrated fault. *Journal of Geophysical Research*, *100*, 22,155–22,173.

Segall, P., Rubin, A. M., Bradley, A. M., & Rice, J. R. (2010). Dilatant strengthening as a mechanism for slow slip events. *Journal of Geophysical Research*, *115*, B12305. https://doi.org/10.1029/2010JB007449

Shelly, D. R. (2010). Periodic, chaotic, and doubled earthquake recurrence intervals on the deep San Andreas Fault. *Science*, *328*, 1385–1388.

Shelly, D. R. (2017). A 15 year catalog of more than 1 million low-frequency earthquakes: Tracking tremor and slip along the deep San Andreas Fault. *Journal of Geophysical Research: Solid Earth*, *122*, 3739–3753. https://doi.org/10.1002/2017JB014047

Shelly, D. R., Beroza, G. C., & Ide, S. (2007). Non-volcanic tremor and low-frequency earthquake swarms. *Nature*, *446*, 305–307. https://doi.org/10.1038/nature05666

Shelly, D. R., & Hardebeck, J. L. (2010). Precise tremor source locations and amplitude variations along the lower-crustal central San Andreas Fault. *Geophysical Research Letters*, *37*, L14301. https://doi.org/10.1029/2010GL043672

Shelly, D. R., & Johnson, K. M. (2011). Tremor reveals stress shadowing, deep postseismic creep, and depth-dependent slip recurrence on the lower-crustal San Andreas Fault near Parkfield. *Geophysical Research Letters*, *381*, L13312. https://doi.org/10.1029/2011GL047863

Skarbek, R. M., Rempel, A. W., & Schmidt, D. A. (2012). Geologic heterogeneity can produce aseismic slip transients. *Geophysical Research Letters*, *39*, L21306. https://doi.org/10.1029/2012GL053762

Skarbek, R. M., Rempel, A. W., & Thomas, A. M. (2014). Effects of tidal modulation in heterogeneous models of slow slip, American Geophysical Union, Fall Meeting 2014, Abstract S53C-4541.

Thomas, A. M., Beeler, N. M., Bletery, Q., Burgmann, R., & Shelly, D. (2017). Using low frequency earthquake families on the San Andreas Fault as deep creepmeters. *Journal of Geophysical Research*, *122*. https://doi.org/10.1002/2017JB014404

Thomas, A. M., Burgmann, R., Shelly, D. R., Beeler, N. M., & Rudolph, M. L. (2012). Tidal sensitivity of low frequency earthquakes near Parkfield, CA: Implications for fault mechanics within the brittle-ductile transition. *Journal of Geophysical Research*, *117*, B05301. https://doi.org/10.1029/2011JB009036

Thomas, A. M., Nadeau, R. M., & Burgmann, R. (2009). Tremor-tide correlations and near-lithostatic pore pressure on the deep San Andreas Fault. *Nature*, *462*. https://doi.org/10.1038/nature08654

Walder, J., & Nur, A. (1984). Porosity reduction and crustal pore pressure development. *Journal of Geophysical Research*, *89*, 11,539–11,548.

Wang, K., & He, J. (1999). Mechanics of low-stress forearcs: Nankai and Cascadia. *Journal of Geophysical Research*, *104*, 15,191–15,205.

Yabe, S., Tanaka, Y., Houston, H., & Ide, S. (2015). Tidal sensitivity of tectonic tremors in Nankai and Cascadia subduction zones. *Journal of Geophysical Research: Solid Earth*, *120*, 7587–7605. https://doi.org/10.1002/2015JB012250